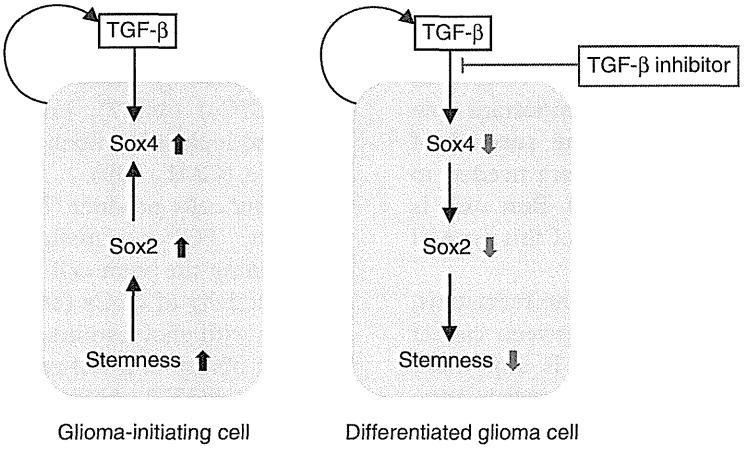

Figure 4. Effects of the TGF-β–Smad–Sox4–Sox2 axis on the maintenance of GIC stemness. TGF-β directly induces Sox4 expression. Subsequently, Sox4 promotes Sox2 expression, which plays significant roles in sustaining GIC stemness. TGF-β inhibitor blocks this TGF-β–Sox4–Sox2 axis, promotes GIC differentiation, and deprives these cells of their aggressiveness. Differentiated glioma cells (right panel) may be more sensitive to conventional chemotherapy and radiotherapy than undifferentiated GICs (left panel).

negative effects on cancer progression. The bidirectional roles of TGF-β can be observed at the molecular, cellular, and tissue levels. Although we described the positive effects of TGF-β on maintaining the stemness of cancer-initiating cells, TGF-β has also been shown to decrease the number of specific types of cancer-initiating cells, including diffuse-type gastric carcinoma cells (52). Moreover, TGF-β induces maintenance of stem cell-like properties of certain breast cancer-initiating cells (48), while suppression of the TGF-β pathway leads to an increase in breast cancer-initiating cells in other types of breast cancer cells (53), thereby suggesting that the response to TGF-β varies depending on the type of cancer-initiating cells.

Mani et al. (48) reported that TGF-β maintains stem cell-like properties of certain cancer-initiating cells through induction of EMT. They showed that normal and transformed mammary epithelial cells acquired stem cell-like properties with high tumorigenic activity when EMT was induced in these cells by TGF-β. Although we have not determined whether the sizes of cancer-initiating cell compartments are affected by EMT in the pancreatic carcinoma Panc1 cells and lung adenocarcinoma A549 cells described above, these findings suggest a functional connection between EMT and cancer-initiating properties of certain epithelial cells.

Recent findings based on genome-wide analyses of Smad-binding sites in some types of cells, which were performed using ChIP-sequencing analyses, revealed that the binding profiles of Smads differ remarkably depending on the cell types and are affected by interaction with transcription factors expressed in each cell type and by cell-specific differences in baseline chromatin accessibility patterns (7,9,54). It is thus possible that the response of cells to TGF-β may be differentially affected by coexisting transcription factors and chromatin assembly patterns. Further studies examining global gene expression profiles and genome-wide maps of protein binding sites or epigenetic marks using high-throughput sequencing may be valuable for elucidating the mechanisms of differential cellular responsiveness to TGF-β.

Acknowledgements

This work was supported by KAKENHI (grants-in-aid for scientific research on Innovative Area (Integrative Research on Cancer Microenvironment Network; grant number 22112002)) and for Young Scientists (B) (grant numbers 22700876 (S.E.) and 22790750 (D.K.)); the Global Center of Excellence Program (Integrative Life Science Based on the Study of Biosignaling Mechanisms) from the Ministry of Education, Culture, Sports, Science and Technology (MEXT), Japan; a Grant-in-Aid for Cancer Research for the Third-Term Comprehensive 10-Year Strategy for Cancer Control (H22-013) from the Ministry of Health, Labour and Welfare of Japan; and a grant from Swedish Cancer Society (grant number 10 0452).

Declaration of interest: K.M. is supported by a research fund from Antisense Pharma GmbH (Germany). The authors alone are responsible for the content and writing of the paper.

References

1. Moses HL, Roberts AB. The discovery of TGF-β: a historical perspective. The TGF-β family. New York: Cold Spring Harbor Laboratory Press; 2009. p. 1–28.

2. Roberts AB, Wakefield LM. The two faces of transforming growth factor-β in carcinogenesis. Proc Natl Acad Sci USA. 2003;100:8621–3.
3. Ikushima H, Miyazono K. TGF-β signalling: a complex web in cancer progression. Nat Rev Cancer. 2010;10:415–24.
4. Sanchez-Capelo A. Dual role for TGF-β1 in apoptosis. Cytokine Growth Factor Rev. 2005;16:15–34.
5. Heldin CH, Miyazono K, ten Dijke P. TGF-β signalling from cell membrane to nucleus through SMAD proteins. Nature. 1997;390:465–71.
6. Miyazono K, Kamiya Y, Morikawa M. Bone morphogenetic protein receptors and signal transduction. J Biochem. 2010; 147:35–51.
7. Koinuma D, Tsutsumi S, Kamimura N, Taniguchi H, Miyazawa K, Sunamura M, et al. Chromatin immunoprecipitation on microarray analysis of Smad2/3 binding sites reveals roles of ETS1 and TFAP2A in transforming growth factor β signaling. Mol Cell Biol. 2009;29:172–86.
8. Koinuma D, Tsutsumi S, Kamimura N, Imamura T, Aburatani H, Miyazono K. Promoter-wide analysis of Smad4 binding sites in human epithelial cells. Cancer Sci. 2009;100:2133–42.
9. Mizutani A, Koinuma D, Tsutsumi S, Kamimura N, Morikawa M, Suzuki HI, et al. Cell type-specific target selection by combinatorial binding of Smad2/3 proteins and hepatocyte nuclear factor 4α in HepG2 cells. J Biol Chem. 2011; 286:29848–60.
10. Kamiya Y, Miyazono K, Miyazawa K. Smad7 inhibits transforming growth factor-β family type I receptors through two distinct modes of interaction. J Biol Chem. 2010;285: 30804–13.
11. Deheuninck J, Luo K. Ski and SnoN, potent negative regulators of TGF-β signaling. Cell Res. 2009;19:47–57.
12. Moustakas A, Heldin CH. Non-Smad TGF-β signals. J Cell Sci. 2005;118:3573–84.
13. Lee MK, Pardoux C, Hall MC, Lee PS, Warburton D, Qing J, et al. TGF-β activates Erk MAP kinase signalling through direct phosphorylation of ShcA. EMBO J. 2007;26: 3957–67.
14. Thiery JP, Acloque H, Huang RY, Nieto MA. Epithelial-mesenchymal transitions in development and disease. Cell. 2009;139:871–90.
15. Sabe H. Cancer early dissemination: cancerous epithelial-mesenchymal transdifferentiation and transforming growth factor-β signalling. J Biochem. 2011;149:633–9.
16. Zeisberg M, Neilson EG. Biomarkers for epithelial-mesenchymal transitions. J Clin Invest. 2009;119:1429–37.
17. Miyazono K. Transforming growth factor-β signaling in epithelial-mesenchymal transition and progression of cancer. Proc Jpn Acad Ser B Phys Biol Sci. 2009;85:314–23.
18. Shirakihara T, Horiguchi K, Miyazawa K, Ehata S, Shibata T, Morita I, et al. TGF-β regulates isoform switching of FGF receptors and epithelial-mesenchymal transition. EMBO J. 2011;30:783–95.
19. Itoh N, Ornitz DM. Fibroblast growth factors: from molecular evolution to roles in development, metabolism and disease. J Biochem. 2011;149:121–30.
20. Horiguchi K, Sakamoto K, Koinuma D, Semba K, Inoue A, Inoue S, et al. TGF-β drives epithelial-mesenchymal transition through δEF1-mediated downregulation of ESRP. Oncogene. 2011 Oct 31 (Epub ahead of print).
21. Warzecha CC, Jiang P, Amirikian K, Dittmar KA, Lu H, Shen S, et al. An ESRP-regulated splicing programme is abrogated during the epithelial-mesenchymal transition. EMBO J. 2010;29:3286–30.
22. Horiguchi K, Shirakihara T, Nakano A, Imamura T, Miyazono K, Saitoh M. Role of Ras signaling in the induction of snail by transforming growth factor-β. J Biol Chem. 2009; 284:245–53.
23. Matsuzaki K. Smad phosphoisoform signals in acute and chronic liver injury: similarities and differences between epithelial and mesenchymal cells. Cell Tissue Res. 2011 May 31 (Epub ahead of print).
24. Minoo P, Su G, Drum H, Bringas P, Kimura S. Defects in tracheoesophageal and lung morphogenesis in Nkx2.1-/- mouse embryos. Dev Biol. 1999;209:60–71.
25. Weir BA, Woo MS, Getz G, Perner S, Ding L, Beroukhim R, et al. Characterizing the cancer genome in lung adenocarcinoma. Nature. 2007;450:893–8.
26. Winslow MM, Dayton TL, Verhaak RG, Kim-Kiselak C, Snyder EL, Feldser DM, et al. Suppression of lung adenocarcinoma progression by Nkx2-1. Nature. 2011;473: 101–4.
27. Saito RA, Watabe T, Horiguchi K, Kohyama T, Saitoh M, Nagase T, et al. Thyroid transcription factor-1 inhibits transforming growth factor-β-mediated epithelial-to-mesenchymal transition in lung adenocarcinoma cells. Cancer Res. 2009;69: 2783–91.
28. Minoo P, Hu L, Zhu N, Borok Z, Bellusci S, Groffen J, et al. SMAD3 prevents binding of NKX2.1 and FOXA1 to the SpB promoter through its MH1 and MH2 domains. Nucleic Acids Res. 2008;36:179–88.
29. Kang Y, Siegel PM, Shu W, Drobnjak M, Kakonen SM, Cordon-Cardo C, et al. A multigenic program mediating breast cancer metastasis to bone. Cancer Cell. 2003;3:537–49.
30. Komuro A, Yashiro M, Iwata C, Morishita Y, Johansson E, Matsumoto Y, et al. Diffuse-type gastric carcinoma: progression, angiogenesis, and transforming growth factor β signaling. J Natl Cancer Inst. 2009;101:592–604.
31. Johansson E, Komuro A, Iwata C, Hagiwara A, Fuse Y, Watanabe A, et al. Exogenous introduction of tissue inhibitor of metalloproteinase 2 reduces accelerated growth of TGF-β-disrupted diffuse-type gastric carcinoma. Cancer Sci. 2010;101:2398–403.
32. Watabe T, Nishihara A, Mishima K, Yamashita J, Shimizu K, Miyazawa K, et al. TGF-β receptor kinase inhibitor enhances growth and integrity of embryonic stem cell-derived endothelial cells. J Cell Biol. 2003;163:1303–11.
33. Kokudo T, Suzuki Y, Yoshimatsu Y, Yamazaki T, Watabe T, Miyazono K. Snail is required for TGF-β-induced endothelial-mesenchymal transition of embryonic stem cell-derived endothelial cells. J Cell Sci. 2008;121:3317–24.
34. Padua D, Zhang XH, Wang Q, Nadal C, Gerald WL, Gomis RR, et al. TGFβ primes breast tumors for lung metastasis seeding through angiopoietin-like 4. Cell. 2008; 133:66–77.
35. Yang YA, Dukhanina O, Tang B, Mamura M, Letterio JJ, MacGregor J, et al. Lifetime exposure to a soluble TGF-β antagonist protects mice against metastasis without adverse side effects. J Clin Invest. 2002;109:1607–15.
36. Yoshimura A, Wakabayashi Y, Mori T. Cellular and molecular basis for the regulation of inflammation by TGF-β. J Biochem. 2010;147:781–92.
37. Flavell RA, Sanjabi S, Wrzesinski SH, Licona-Limon P. The polarization of immune cells in the tumour environment by TGF-β. Nat Rev Immunol. 2010;10:554–67.
38. Nam JS, Terabe M, Mamura M, Kang MJ, Chae H, Stuelten C, et al. An anti-transforming growth factor-β antibody suppresses metastasis via cooperative effects on multiple cell compartments. Cancer Res. 2008;68:3835–43.

39. Azuma H, Ehata S, Miyazaki H, Watabe T, Maruyama O, Imamura T, et al. Effect of Smad7 expression on metastasis of mouse mammary carcinoma JygMC(A) cells. J Natl Cancer Inst. 2005;97:1734–46.
40. Ehata S, Hanyu A, Hayashi M, Aburatani H, Kato Y, Fujime M, et al. Transforming growth factor-β promotes survival of mammary carcinoma cells through induction of antiapoptotic transcription factor DEC1. Cancer Res. 2007; 67:9694–703.
41. Li Y, Xie M, Yang J, Yang D, Deng R, Wan Y, et al. The expression of antiapoptotic protein survivin is transcriptionally upregulated by DEC1 primarily through multiple Sp1 binding sites in the proximal promoter. Oncogene. 2006;25:3296–306.
42. Hoshino Y, Katsuno Y, Ehata S, Miyazono K. Autocrine TGF-β protects breast cancer cells from apoptosis through reduction of BH3-only protein, Bim. J Biochem. 2011;149: 55–65.
43. Yin JJ, Selander K, Chirgwin JM, Dallas M, Grubbs BG, Wieser R, et al. TGF-β signaling blockade inhibits PTHrP secretion by breast cancer cells and bone metastases development. J Clin Invest. 1999;103:197–206.
44. Deckers M, van Dinther M, Buijs J, Que I, Lowik C, van der Pluijm G, et al. The tumor suppressor Smad4 is required for transforming growth factor β-induced epithelial to mesenchymal transition and bone metastasis of breast cancer cells. Cancer Res. 2006;66:2202–9.
45. Ehata S, Hanyu A, Fujime M, Katsuno Y, Fukunaga E, Goto K, et al. Ki26894, a novel transforming growth factor-β type I receptor kinase inhibitor, inhibits in vitro invasion and in vivo bone metastasis of a human breast cancer cell line. Cancer Sci. 2007;98:127–33.
46. Ikushima H, Todo T, Ino Y, Takahashi M, Miyazawa K, Miyazono K. Autocrine TGF-β signaling maintains tumorigenicity of glioma-initiating cells through Sry-related HMG-box factors. Cell Stem Cell. 2009;5:504–14.
47. Penuelas S, Anido J, Prieto-Sanchez RM, Folch G, Barba I, Cuartas I, et al. TGF-β increases glioma-initiating cell self-renewal through the induction of LIF in human glioblastoma. Cancer Cell. 2009;15:315–27.
48. Mani SA, Guo W, Liao MJ, Eaton EN, Ayyanan A, Zhou AY, et al. The epithelial-mesenchymal transition generates cells with properties of stem cells. Cell. 2008;133:704–15.
49. Naka K, Hoshii T, Muraguchi T, Tadokoro Y, Ooshio T, Kondo Y, et al. TGF-β-FOXO signalling maintains leukaemia-initiating cells in chronic myeloid leukaemia. Nature. 2010;463:676–80.
50. Ferletta M, Caglayan D, Mokvist L, Jiang Y, Kastemar M, Uhrbom L, et al. Forced expression of Sox21 inhibits Sox2 and induces apoptosis in human glioma cells. Int J Cancer. 2011;129:45–60.
51. Anido J, Saez-Borderias A, Gonzalez-Junca A, Rodon L, Folch G, Carmona MA, et al. TGF-β receptor inhibitors target the CD44(high)/Id1(high) glioma-initiating cell population in human glioblastoma. Cancer Cell. 2010;18:655–68.
52. Ehata S, Johansson E, Katayama R, Koike S, Watanabe A, Hoshino Y, et al. Transforming growth factor-β decreases the cancer-initiating cell population within diffuse-type gastric carcinoma cells. Oncogene. 2011;30:1693–705.
53. Tang B, Yoo N, Vu M, Mamura M, Nam JS, Ooshima A, et al. Transforming growth factor-β can suppress tumorigenesis through effects on the putative cancer stem or early progenitor cell and committed progeny in a breast cancer xenograft model. Cancer Res. 2007;67:8643–52.
54. Morikawa M, Koinuma D, Tsutsumi S, Vasilaki E, Kanki Y, Heldin CH, et al. ChIP-seq reveals cell type-specific binding patterns of BMP-specific Smads and a novel binding motif. Nucleic Acids Res. 2011;39:8712–27.

The EMBO Journal (2012) 31, 2541–2552 | © 2012 European Molecular Biology Organization | All Rights Reserved 0261-4189/12
www.embojournal.org

THE EMBO JOURNAL

Structure of a dominant-negative helix-loop-helix transcriptional regulator suggests mechanisms of autoinhibition

Ryohei Ishii[1,8], Kazunobu Isogaya[2,8], Azusa Seto[3,8], Daizo Koinuma[2,8], Yuji Watanabe[3], Fumio Arisaka[4], So-ichi Yaguchi[5], Hiroaki Ikushima[2], Naoshi Dohmae[6,7], Kohei Miyazono[2], Keiji Miyazawa[2,5,*], Ryuichiro Ishitani[1,7] and Osamu Nureki[1,*]

[1]Department of Biophysics and Biochemistry, Graduate School of Science, The University of Tokyo, Bunkyo-ku, Tokyo, Japan, [2]Department of Molecular Pathology, Graduate School of Medicine, The University of Tokyo, Bunkyo-ku, Tokyo, Japan, [3]Department of Basic Medical Sciences, Institute of Medical Science, The University of Tokyo, Minato-ku, Tokyo, Japan, [4]Department of Biological Information, Graduate School of Bioscience and Biotechnology, Tokyo Institute of Technology, Yokohama, Kanagawa, Japan, [5]Department of Biochemistry, Interdisciplinary Graduate School of Medicine and Engineering, University of Yamanashi, Chuo, Yamanashi, Japan, [6]Biomolecular Characterization Team, RIKEN, Wako, Saitama, Japan and [7]Advanced Science Institute, RIKEN, Wako, Saitama, Japan

Helix-loop-helix (HLH) family transcription factors regulate numerous developmental and homeostatic processes. Dominant-negative HLH (dnHLH) proteins lack DNA-binding ability and capture basic HLH (bHLH) transcription factors to inhibit cellular differentiation and enhance cell proliferation and motility, thus participating in patho-physiological processes. We report the first structure of a free-standing human dnHLH protein, HHM (Human homologue of murine maternal Id-like molecule). HHM adopts a V-shaped conformation, with N-terminal and C-terminal five-helix bundles connected by the HLH region. In striking contrast to the common HLH, the HLH region in HHM is extended, with its hydrophobic dimerization interfaces embedded in the N- and C-terminal helix bundles. Biochemical and physicochemical analyses revealed that HHM exists in slow equilibrium between this V-shaped form and the partially unfolded, relaxed form. The latter form is readily available for interactions with its target bHLH transcription factors. Mutations disrupting the interactions in the V-shaped form compromised the target transcription factor specificity and accelerated myogenic cell differentiation. Therefore, the V-shaped form of HHM may represent an autoinhibited state, and the dynamic conformational equilibrium may control the target specificity.

The EMBO Journal (2012) **31**, 2541–2552. doi:10.1038/emboj.2012.77; Published online 27 March 2012
Subject Categories: chromatin & transcription; structural biology
Keywords: carcinogenesis; TGF-β signal; transcription factor; X-ray crystallography

Introduction

The helix-loop-helix (HLH) proteins are central regulators in a wide variety of developmental and homeostatic processes (Olson and Klein, 1994). Especially, basic helix-loop-helix (bHLH) transcription factors play key roles in regulating gene expression, cell cycle control, and developmental processes, by binding to the 'E box' in the promoters of tissue-specific genes through homo- and heterodimer formation (Murre *et al*, 1989; Blackwell *et al*, 1990; Kreider *et al*, 1992; Zebedee and Hara, 2001). The HLH proteins are divided into seven classes, based on the presence of a DNA-binding region as well as other appended motifs/domains (Massari and Murre, 2000). The class-I bHLH proteins, such as E12, E47, HEB, and E2-2, are ubiquitously expressed in many tissues. In contrast, the class-II bHLH proteins, such as MyoD, NeuroD, and Hes, exhibit tissue-specific expression and form heterodimers with the class-I bHLH proteins to regulate distinct developmental pathways, such as myogenesis, neurogenesis and lymphopoiesis (Weintraub *et al*, 1990; Lassar *et al*, 1991; Weintraub *et al*, 1991; Weintraub, 1993; Parkhurst and Meneely, 1994; Lee *et al*, 1995; Shen and Kadesch, 1995; Ma *et al*, 1996; Rawls and Olson, 1997). The class-III HLH proteins include the Myc family of transcription factors, which contain a leucine zipper (LZ) adjacent to the HLH motif. The class-IV HLH proteins include Mad, Max, and Mxi, which are capable of dimerizing with the Myc proteins and with each other (Blackwood and Eisenman, 1991; Ayer *et al*, 1993; Zervos *et al*, 1993). The class-V HLH proteins are represented by the Id family proteins (Id1, Id2, Id3, and Id4), which do not contain the basic region prior to the HLH motif and lack DNA-binding ability. The Id family proteins form heterodimers with the bHLH proteins, and inhibit their functions in a dominant-negative manner (Benezra *et al*, 1990; Sun *et al*, 1991; Yokota and Mori, 2002; Perk *et al*, 2005). The class-VI HLH proteins specifically contain a Pro residue in their basic region (Klambt *et al*, 1989; Rushlow *et al*, 1989). The class-VII HLH proteins are characterized by the bHLH–PAS domain, and include the aromatic hydrocarbon receptor and its nuclear translocator, as well as HIF1α, SIM, AhR, ARNT, and circadian clock-related factors (Crews, 1998).

The Id family proteins of the dominant-negative class-V HLH (dnHLH) have attracted strong medical interest, based on the findings that deregulated Id activity is tumourigenic

*Corresponding authors. K Miyazawa, Department of Biochemistry, Interdisciplinary Graduate School of Medicine and Engineering, University of Yamanashi, 1110 Shimokato, Chuo, Yamanashi 409-3898, Japan. Tel.: +81 55 273 6784; Fax: +81 55 273 6784; E-mail: kmiyazawa@yamanashi.ac.jp or O Nureki, Department of Biophysics and Biochemistry, Graduate School of Science, The University of Tokyo, 2-11-16 Yayoi, Bunkyo-ku, Tokyo 113-0032, Japan. Tel.: +81 3 5841 4392; Fax: +81 3 5841 8057; E-mail: nureki@biochem.s.u-tokyo.ac.jp
[8]These authors contributed equally to this work

Received: 1 May 2011; accepted: 6 March 2012; published online 27 March 2012

©2012 European Molecular Biology Organization

and contributes to malignancy, such as loss of differentiation, unrestricted proliferation, enhanced cell motility, and neoangiogenesis (Perk *et al*, 2005). Elevated expression of Id genes has been observed in carcinomas of various origins as well as melanomas and leukaemias (Ishiguro *et al*, 1995; Fong *et al*, 2004; Han *et al*, 2004; Wang *et al*, 2004). While the Id genes themselves are not canonical oncogenes, their overexpression affects key oncogenic pathways involving Ras, Myc, and ETS (Perk *et al*, 2005). However, the structures of the Id proteins and the mechanisms controlling their activities have remained unclear.

Human homologue of murine maternal Id-like molecule (HHM), also known as cyclin D1-binding protein (DIP1), is a member of the dnHLH family, but it is larger than the Ids and includes a putative LZ motif and an acidic C-terminal region (Terai *et al*, 2000). By definition, HHM associates with cyclin D1 to regulate the G1/S-phase progression of hepatocytes, probably through the Rb pathway (Xia *et al*, 2000). Intriguingly, HHM exerts opposite effects on cells, depending on the cellular contexts. HHM was shown to be involved in the growth regulation of hepatocytes and the progression of hepatocellular carcinomas. In HHM-knockout mice, liver regeneration after partial hepatectomy was attenuated, as compared with that in wild-type mice (Ma *et al*, 2006). In addition, HHM expression is increased in the early phases of hepatocarcinogenesis, and HHM accelerates S-phase entry in HepG2 hepatocellular carcinoma cells (Terai *et al*, 2000). These observations indicate positive regulatory roles of HHM in proliferation of liver cells. In contrast, HHM-knockout mice often develop liver tumours (Sonnenberg-Riethmacher *et al*, 2007), and transgenic mice overexpressing HHM in the liver are less susceptible to chemical hepatocarcinogenesis (Ma *et al*, 2006). These observations indicate that HHM has tumour-suppressor functions in the liver. However, the mechanism underlying these opposite roles of HHM in the regulation of cell proliferation and tumour progression, which are dependent on the cellular context, remains to be elucidated. Recently, HHM was found to disrupt the physical interaction of specific transcription factors with R-Smads, to inhibit TGF-β signalling in a cellular response-specific manner (Ikushima *et al*, 2008). Oligodendrocyte transcription factor 1 (Olig1), a class-II bHLH protein, was identified as one of the Smad-binding transcription factors inhibited by HHM (Ikushima *et al*, 2008). We have observed that Olig1 regulates the expression of the TGF-β controlled genes that enhance cell motility and migration (Motizuki M & Miyazawa K, unpublished results). In contrast to the Id proteins, which interact with the ubiquitously expressed class-I bHLH transcription factors, HHM associates with the tissue-specific class-II bHLH transcription factor Olig1 to regulate Smad-dependent transcription, suppressing tumour progression.

To understand the regulation mechanism of the dnHLH proteins, we solved the crystal structure of full-length HHM at 2.5 Å resolution. This is the first structure of a dnHLH, as well as the first presentation of the free-form of an HLH transcription regulator, devoid of its dimeric counterpart. The HHM structure adopts a V-shaped conformation composed of N- and C-terminal five-helix bundles. The hydrophobic dimerization interfaces of the HLH region are embedded in these helix bundles, and are thereby protected from nonspecific interactions. Combined with biochemical, physicochemical, and cell biological analyses, we propose that the present crystal structure of HHM represents an autoinhibited state, and the slow equilibrium with the partially unfolded conformation enables the fine-tuning of the specificity for the target transcription factor.

Results and Discussion

Structure determination

The crystal structure of HHM (360 residues, molecular weight 40 kDa) was determined by the multiple anomalous diffraction method, using a selenomethionine-labelled crystal. We first obtained experimental phases to 4.0 Å resolution using a SeMet-labelled crystal, as previously described (Seto *et al*, 2009), but the quality of the resulting electron density map was quite low and the assignment of the amino-acid residues was virtually impossible. The addition of a sulfhydryl-specific reagent, *p*-chloromercuribenzoic acid (PCMB), to the protein sample prior to crystallization improved the resolution of the crystal to 3.5 Å, which enabled the preliminary interpretation of the electron density map. The exposed Cys residues may disturb the crystal packing, thus reducing the crystal quality. On the basis of this preliminary structural model, we substituted the Cys residues exposed on the molecular surface (Cys198 and Cys300; Supplementary Figure S1) with Ser, which further improved the resolution to 2.5 Å. The final model was refined against the diffraction data extending to 2.5 Å resolution with crystallographic $R/R_{free} = 22.2/26.1\%$, by refinement of the individual B-factor and TLS tensor parameters. The model contains one molecule in the asymmetric unit, in which residues 1–15, 41–44, 139–150, 201–228, and 329–333 are structurally disordered.

Overall structure

HHM adopts an all α-helical structure consisting of two-helix bundles, which are arranged in a V-shaped conformation (Figure 1). Hereafter, we divide the HHM structure into the following three regions: the N-terminal helix bundle (N-bundle, residues 16–138), the HLH region (residues 151–200), and the C-terminal helix bundle (C-bundle, residues 229–360; Figure 1). The HLH region of HHM shares sequence homology with the other HLH proteins and consists of helices α5 and α6, which correspond to the first and second α-helices, respectively, of the canonical HLH motif and are connected by the short loop L5. The N-bundle consists of helices α1 to α4 and forms extensive hydrophobic interactions with helix α5 of the HLH region (Figure 2A). The C-bundle consists of helices α7 to α10 and forms extensive hydrophobic interactions with helix α6 of the HLH region (Figure 2B). The loop regions connecting the N-bundle (residues 139–150) and the C-bundle (residues 201–228) to the HLH region are structurally disordered.

Previous studies suggested that the acidic domain and the putative LZ motif immediately follow the HLH motif, and these regions of HHM may be involved in intermolecular interactions (Hwang *et al*, 1997; Terai *et al*, 2000). This acidic domain is included in loop L6, which is between the HLH region and the C-bundle, and is mostly disordered in the present crystal structure. Moreover, the conserved Leu and Ser/Cys residues (Leu240, Leu247, Cys254, and Leu261) in this putative LZ motif on helix α7 participate in hydrophobic

 ©2012 European Molecular Biology Organization

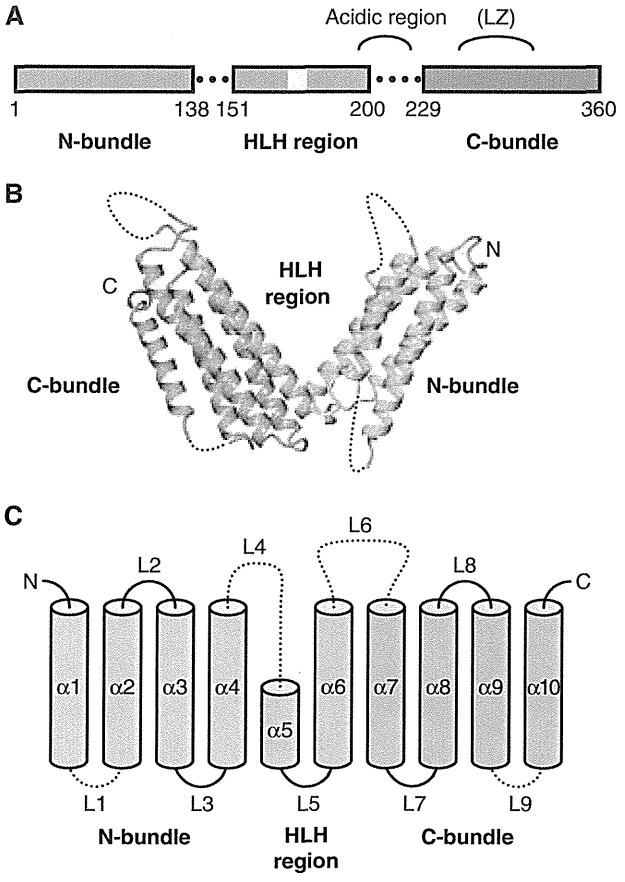

Figure 1 Structure of HHM. (**A**) Schematic representation of the HHM domain architecture. (**B**) Overall structure of HHM. (**C**) Schematic diagram of the secondary structures of HHM. In all of the panels, the same colour code as in panel **A** is used.

interactions with the core of the C-bundle, and do not form a canonical LZ structure (Supplementary Figure S2).

Interactions between the HLH and helix bundles in the free-standing HHM

In the present structure of HHM, helix α5 and loop L5 of the HLH region only interact with the N-bundle, while the N terminus of helix α6 forms extensive interactions with both the N- and C-bundles (Figure 2A and C, and Supplementary Figure S3). Especially, the N terminus of helix α6 harbours a sequence conserved in the HHM orthologues from various species, representing the ^{169}NKAAA^{173} motif, which is likely to be important for the interactions between the HLH region and the N- and C-bundles (Figure 2C and D).

This conserved NKAAA motif reinforces the interactions between the N- and C-bundles. The Nδ atom of the Asn169 side chain, which is located at the N terminus of helix α6, hydrogen bonds with the side-chain carboxyl group of Asp275 and the main chain carbonyl oxygen of Val271 in helix α8 of the C-bundle (Figure 2C). On the other hand, the Oδ atom of Asn169 hydrogen bonds with the main chain amide group of Leu114 in helix α4 of the N-bundle (Figure 2C). Furthermore, the side-chain amino group of Lys170 hydrogen bonds with the C-terminal carbonyl oxygen atoms of helix α7 in the C-bundle (Figure 2D). Finally, the side-chain methyl groups of the three consecutive Ala residues (Ala171, Ala172, and Ala173), which form the first turn of helix α6, closely pack against the hydrophobic core of the C-bundle (Figure 2D). Therefore, these interactions seem to be important for HHM to adopt the V-shaped conformation.

In addition to the interactions described above, minor interactions that are independent of the HLH region occur between the N- and C-bundles (Figure 2C). The side-chain carboxyl group of Asp275 hydrogen bonds with the Oγ atom of Thr113 and the main chain amide groups of Ile112 and Thr113. The Cγ atom of Val271 makes a van der Waals contact with the Cα atom of Gly111. Gly111, Val271, and Asp275 are also conserved in the HHM orthologues from various species. These interactions anchor the N termini of helices α4 and α8, thereby stabilizing the V-shaped structure.

Structural comparison between the HLH motifs of HHM and canonical bHLH transcription factors

The canonical structures of the bHLH transcription factors reported to date form homo- or heterodimers through the conserved hydrophobic residues on the amphiphilic α-helices, H1 and H2 (Longo *et al*, 2008; Figure 3A). The C-terminal halves of helices H1 and the N-terminal halves of helices H2 form a short four-helix bundle, while the N-terminal halves of helices H1 provide a basic DNA-binding interface and the C-terminal halves of helices H2 form a two-helix bundle structure (Figure 3B). These dimeric DNA-bound structures of the bHLH transcription factors are considered as the 'active forms', which can activate the transcription of specific genes.

In contrast to these dimeric HLH proteins, the crystal structure of the free-standing HHM revealed that HHM does not form a dimer, and the conserved hydrophobic residues of helices α5 and α6 (corresponding to H1 and H2 in the canonical bHLH, respectively) separately participate in the hydrophobic core formation with the N- and C-bundles (Figure 2A and B). The arrangement of helices α5 and α6 is quite different from that of H1 and H2 observed in the canonical HLH transcription factors (Figures 1B and 3A). There is no contact between helices α5 and α6, whereas helices H1 and H2 of the dimerized HLH transcription factors form intramolecular interactions. Instead, the HLH region of HHM bridges the N- and C-bundles, stabilizing the V-shaped conformation (Figure 1B).

Conservation in the HLH region allows active heterodimer formation in HHM

It is unlikely that the HLH region in the present V-shaped HHM can interact with another HLH protein without undergoing a structural change, as its molecular surface is mainly hydrophilic, and there is no hydrophobic cluster on the surface suitable for the interactions (Supplementary Figure S4). On the basis of the sequence similarity between the bHLH domains of transcription factors and the dnHLH domains of the Id family proteins, the dnHLH and bHLH domains are considered to form a heterodimer, similar to the active forms of the bHLH transcription factors (Wibley *et al*, 1996). By analogy, can the HLH region of HHM also form a similar heterodimer to those of the transcription factors?

Chavali *et al* (2001) proposed some of the important positions for the residues involved in the dimeric stability and the functional specificity of the DNA-bound 'active form' of HLH proteins. Especially, positions 8′ and 11′ in helix H1 and 4″, 5″, 8″, 11″, 12″, 15″, and 19″ in helix H2 are important

©2012 European Molecular Biology Organization

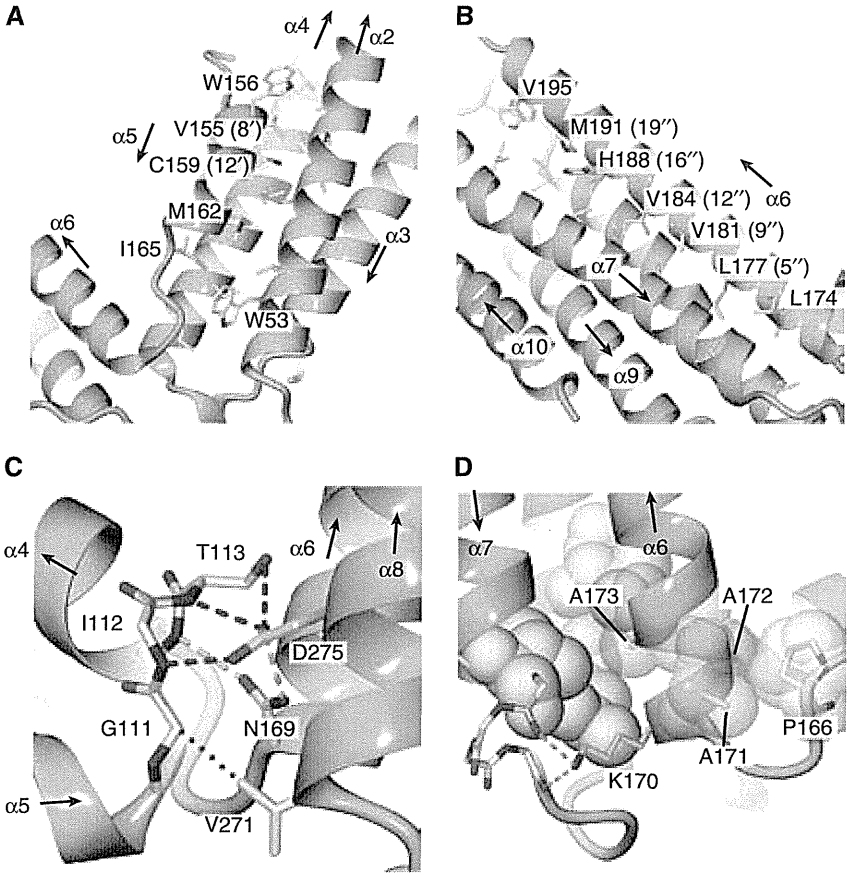

Figure 2 Intramolecular interactions in free-standing HHM. (**A**) Hydrophobic interface between α5 and the N-bundle. (**B**) Hydrophobic interface between α6 and the C-bundle. (**C**) Intramolecular interactions between the N terminus of α6 and the N- and C-bundles at the edge of the V-shape. (**D**) van der Waals interactions involving the conserved NKAAA motif, stabilizing the V-shaped conformation to support the interactions between the HLH region and the N- and C-bundles. In all of the panels, the same colour code as in panel **A** is used.

for the stable packing of the core residues, at the interface of the short four-helix bundle and two-helix bundle structures (Figure 3C). Here, we divided the dimerization interface into five sections, from I to V (Figure 3B and C). These sections are depicted schematically in Figure 3D, using the complex structures of NeuroD1 and E47 (Longo *et al*, 2008) as an example.

The HLH region of HHM shares amino-acid sequence similarity with the bHLH transcription factors, as well as other dnHLH transcriptional regulators (Figure 3C). In HHM, sections I to V are also occupied by similar amino acids to those observed in the canonical HLH proteins (Figure 3E). In sections I and II, positions 4″ and 8″ of HHM are replaced by larger residues (Met and Asn) as compared to the canonical HLH proteins, while the corresponding interaction partners (positions 8′ and 11′) are replaced by smaller residues (Val and Ala; Figure 3D and E). Therefore, upon binding to the target transcription factors, the HLH region of HHM can form the heterodimeric 'active' structure, with the interface stabilized by these complementary residues. Again, it should be noted that these putative interface residues of HHM are involved in the core formation of the N- and C-bundles in the present free-standing structure.

In addition, position 1″ in helix H2 is highly conserved as Lys or Arg in the bHLH transcription factors (Figure 3C), which coincides with the observations that the basic residue at this position interacts with the backbone phosphates of DNA in the reported crystal structures. In contrast, this position is replaced by Ala (the last Ala173 in the NKAAA motif) in HHM. This substitution seems to be reasonable, as HHM no longer interacts with DNA. In the case of Id3, another member of the dnHLH family, this position is occupied by a non-basic Gln residue.

Furthermore, in many HLH proteins, including Myc, Max, and the Id family proteins, the amino-acid sequences of the loop region between helices H1 and H2 also share significant similarity, although they are not directly involved in dimer formation. The third and penultimate positions of the loop region are conserved as small hydrophobic residues (Figure 3C), forming the core of the loop region in the three-dimensional structure (Figure 3A). Thus, these conserved residues are important for the active dimer formation. In HHM, these positions are also conserved as small hydrophobic residues (Ile165 and Ala171). Moreover, the last four residues of the loop region (^{169}NKAA^{174}, the first four residues of the NKAAA motif), which form the N-terminal turn of helix α6 (H2) in the present structure, share considerable sequence similarity with the loop region of the bHLH transcription factors, including v-Myc (EKAA) and Max (EKAS) (Figure 3C). Although HHM is bound to the class-II bHLH transcription factors and thus may correspond to the class-I HLH proteins, we hypothesize that this loop region of HHM may form a similar structure to those of the class-III and IV transcription factors, such as Myc and Max (Nair and Burley,

 ©2012 European Molecular Biology Organization

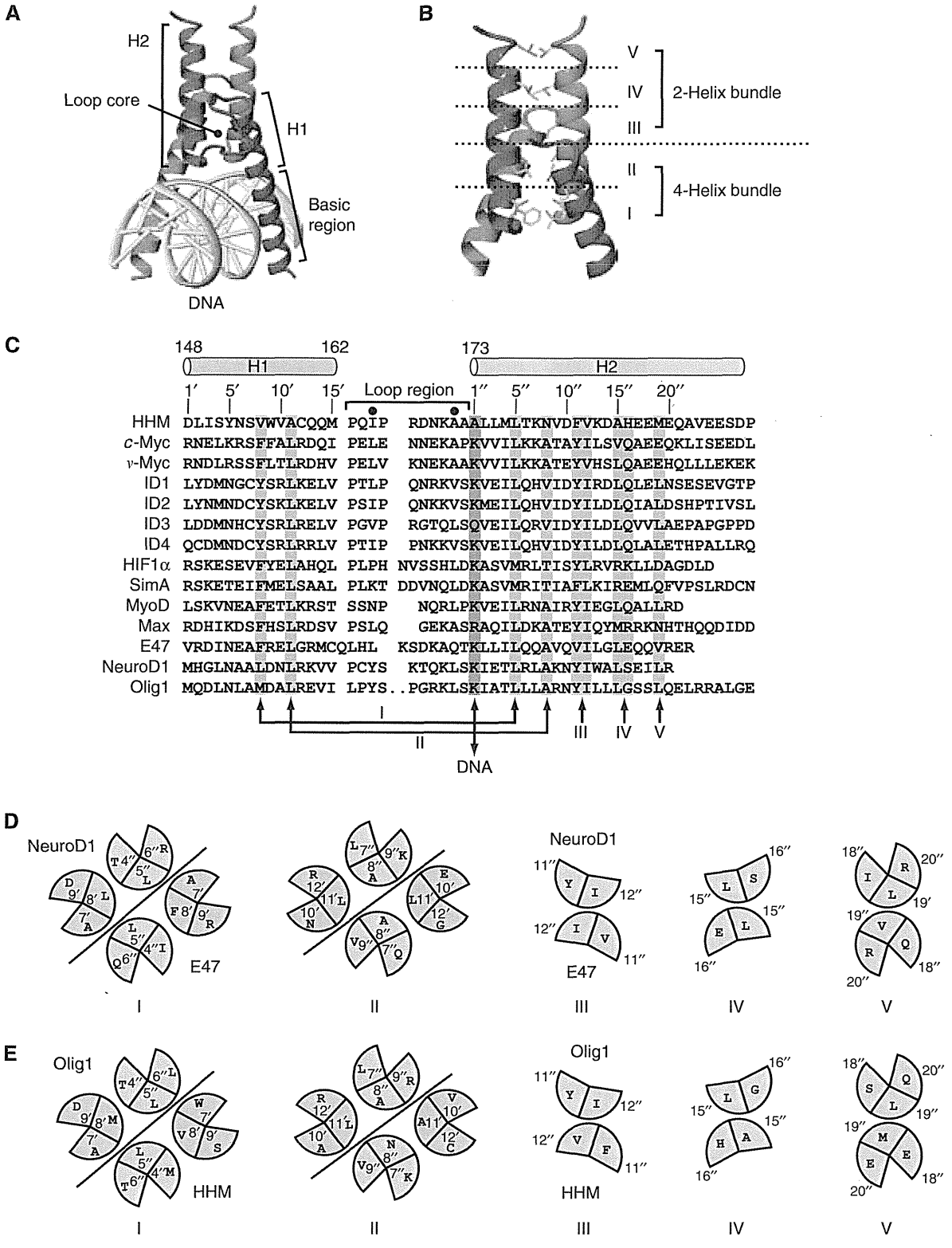

Figure 3 Active dimer formation of HLH proteins. (**A**) The canonical heterodimer structure of the E47 and NeuroD1 bHLH transcription factors bound to DNA. (**B**) Typical dimerization interface of the E47 and NeuroD1 bHLH transcription factor complex, divided into five sections based on the hydrophobic interactions. (**C**) Sequence alignment of HLH proteins. Sections in the dimerization interface are coloured grey. The basic residues that interact with DNA are coloured blue. (**D**) Schematic diagram of each section in the dimerization interface between E47 and NeuroD1. (**E**) Putative schematic diagram of each section in the dimerization interface between HHM and Olig1.

2003). Therefore, the present helical structure (α6) of these four N-terminal residues of HHM may be restructured into the loop conformation upon binding with the target transcription factors.

On the basis of these observations, we constructed a docking model of Olig1–bHLH and the HLH region of HHM (Figure 4A). In HHM, helix H2 is longer than that of the canonical HLH structure, suggesting that the C terminus of

©2012 European Molecular Biology Organization

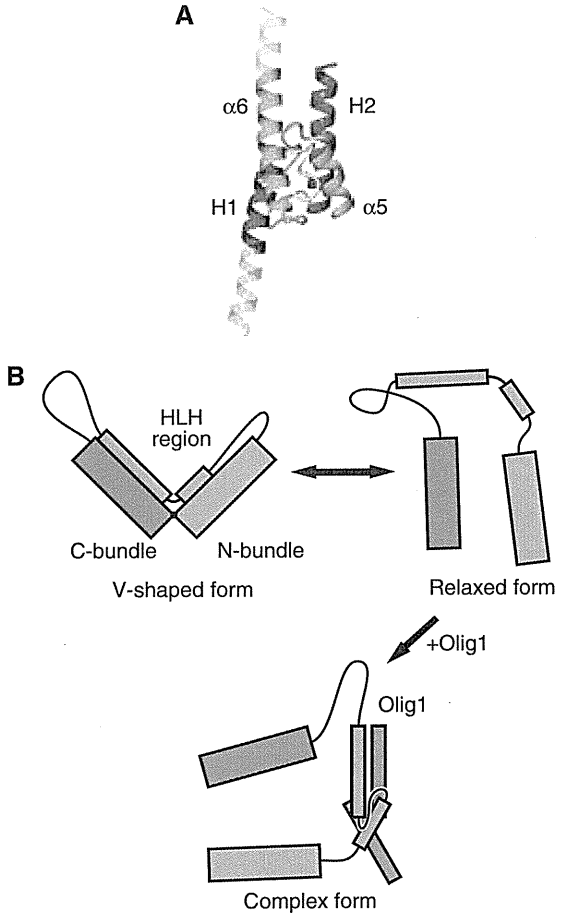

Figure 4 Conformational transition of HHM upon association with the target transcription factors. (**A**) Docking model of Olig1–bHLH and the HLH region of HHM. The regions that are presumably disordered are semitransparent. (**B**) Model of the conformational transition of HHM upon association with and dissociation from the target transcription factors.

helix H2 of HHM may become disordered upon complex formation. Similarly, the basic region of Olig1 in the complex may be disordered without bound DNA. Previous *in vitro* experiments demonstrated that the HLH region of HHM alone is sufficient to exclusively interact with the HLH region of the class-II bHLH transcription factor, Olig1 (Ikushima *et al*, 2008), supporting this docking model. Therefore, although the complex structure of the HLH regions of HHM and Olig1 is still not available, we propose that HHM disrupts the Smads–Olig1 complex by forming an HHM–Olig1 heterodimer via the HLH regions, as in this docking model. Furthermore, this model suggests that the V-shaped form of HHM should undergo a drastic structural change to form this heterodimeric complex.

Equilibrium between the V-shaped and relaxed conformations

To investigate the stability of the V-shaped form of HHM in solution, we incorporated two TEV protease recognition sites into the disordered loops L4 and L6 of the N-terminally GST-tagged HHM (Figure 5A), to enable the separation of the GST-tagged N-bundle, the HLH region, and the C-bundle. We then performed a GST pull-down assay following proteolysis with TEV protease (Figure 5B). If the tertiary interactions between the HLH region and the N- and C-bundles are tight enough to form the stable V-shaped structure, then the C-bundle (and HLH region) will be pulled down together with the GST-tagged N-bundle. Unexpectedly, the HLH region and the C-bundle were not co-precipitated with the N-bundle after the cleavage at loops L4 and L6 (Figure 5B). Although we cannot exclude the possibility that the cleavage of the loops increases the entropy of the unfolded state, this result suggests that the N- and C-bundles and the HLH region spontaneously dissociate, despite the absence of the binding target.

To further investigate the dynamics of the HHM molecule in solution, we performed analytical ultracentrifugation experiments of HHM (Figure 5C and D, and Supplementary Figure S5). The results of the sedimentation velocity experiment revealed the presence of two molecular species, with sedimentation coefficients of 2.6 *S* and 3.3 *S* in solution (Figure 5C, top panel). The sedimentation coefficient depends on both the molecular weight and shape of a protein molecule, and thus the result suggested two possibilities: HHM exists in equilibrium between monomer and dimer, or between two distinctive conformations of monomers. To clarify this point, we further performed sedimentation equilibrium experiments, which would determine the exact molecular weight of the protein. The results indicated that HHM exists as a particle with a molecular weight of 39.4 ± 1.3 kDa (Figure 5D), which is in good agreement with the monomeric mass of HHM calculated from its amino-acid sequence (40.26 kDa). Therefore, these results clearly indicated that the HHM molecule exists in slow equilibrium between two distinctive conformations of monomers, with sedimentation coefficients of 2.6 *S* and 3.3 *S*, respectively.

Next, to identify these HHM conformers, we estimated the sedimentation coefficient of the V-shaped crystal structure of HHM, using the programme HYDROPRO (de la Torre *et al*, 2000). The result indicated that the theoretical sedimentation coefficient of V-shaped HHM is 3.5 *S*, which is consistent with the second peak (i.e., 3.3 *S*) in the sedimentation velocity experiment (Figure 5C, top panel). Furthermore, given the results of the pull-down assay of TEV-cleaved HHM, the first peak may correspond to a partially unfolded conformation, lacking both of the interactions between the HLH region and the N- and C-bundles (Figure 4B). Without these interactions, HHM may adopt a flexible and extended conformation with a higher frictional coefficient, which is consistent with the smaller sedimentation coefficient than that of the V-shaped form. Hereafter, we denote this partially unfolded conformation of HHM as the 'relaxed' form. Taken together, the HHM molecule exists in slow equilibrium between the V-shaped and relaxed forms. In the relaxed form, the HLH region is released from the N- and C-bundles and may readily interact with the target transcription factors, such as Olig1 (Figure 4B).

We also performed MD simulations of the N- and C-bundles lacking the HLH region, which suggested a potential domain rearrangement following the relaxed state of HHM (Supplementary Figure S7 and Supplementary Discussion).

Autoinhibited form of HHM as the transcription regulating factor

On the basis of the results from the above docking model, the pull-down assays, and the ultracentrifugation analyses, the

©2012 European Molecular Biology Organization

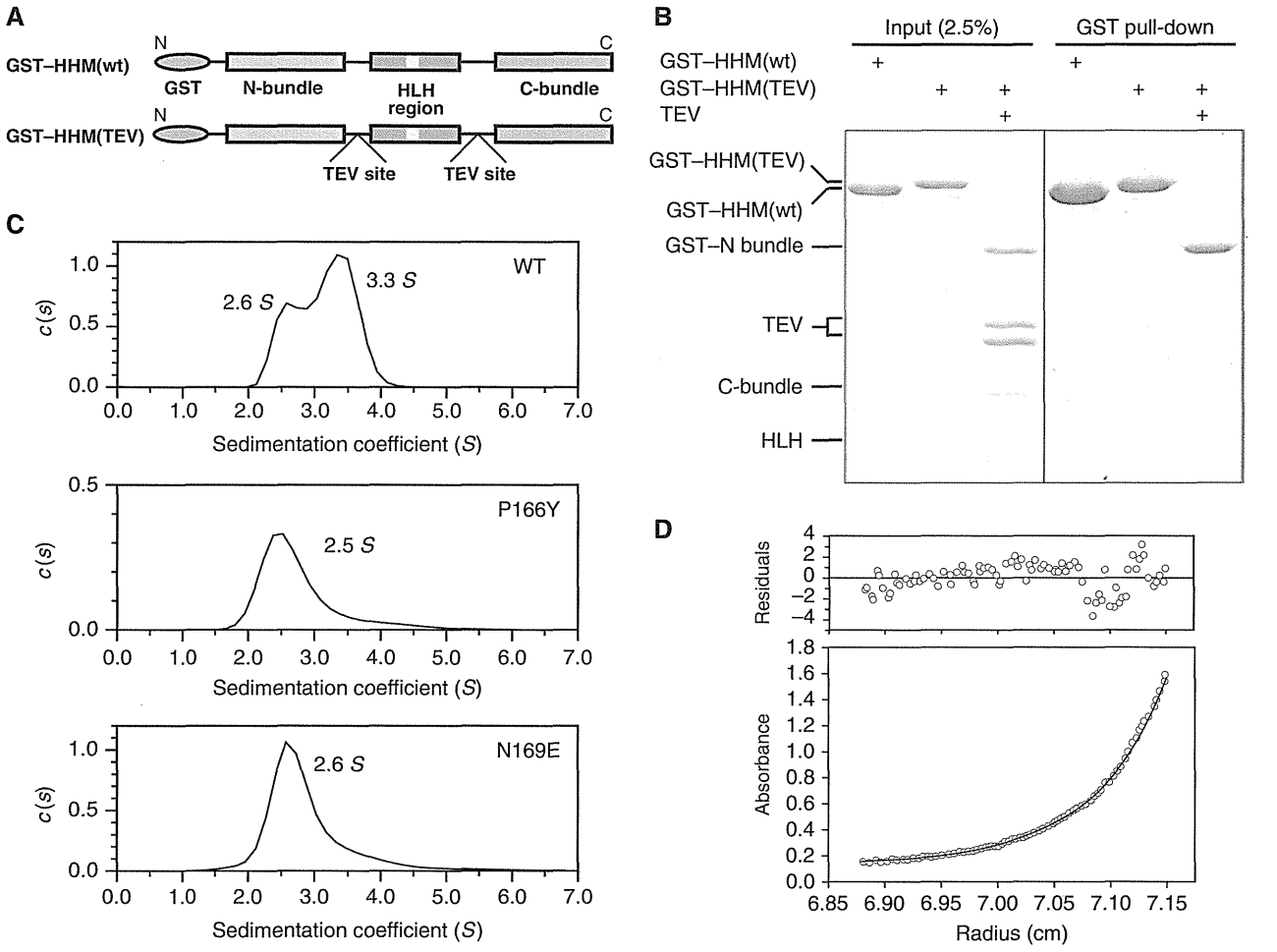

Figure 5 Conformational equilibrium of HHM. (**A**) Schematic representation of the intact GST–HHM and that with TEV sites. (**B**) The GST pull-down assay. After the pull-down, the samples were resolved by SDS–PAGE and the protein bands were stained with Coomassie Brilliant Blue. (**C**) The sedimentation coefficient profiles of wild-type (top), P166Y mutant (middle), and N169E mutant (bottom) HHM. (**D**) Representative results of the sedimentation equilibrium experiment. The absorbance at 280 nm versus the radius and the best-fit curve are shown in the bottom panel. The residuals of the fit from the data are shown in the upper panel.

V-shaped form of HHM may represent an inactive, autoinhibited state. In solution, this V-shaped autoinhibited form of HHM is spontaneously and reversibly converted into the relaxed form, which can readily interact with its target bHLH proteins (Figure 4B, upper panel). Upon binding to class-II bHLH transcription factors, the HLH region of HHM then changes its conformation to adopt the canonical HLH active dimer structure (Figure 4B, lower panel). In the autoinhibited form, the conserved hydrophobic residues in the HLH region, which may compose the molecular interface in the active heterodimeric complex, alternatively interact with the N- and C-bundles to form their hydrophobic cores. Therefore, these N- and C-bundles may act as a cradle to prevent the hydrophobic residues of the HLH region from nonspecifically binding with other proteins. The dynamic equilibrium between the autoinhibited and relaxed forms of HHM may modulate the population of the complex with the target transcription factor, thereby tuning the expression levels of the target genes (Figure 4B).

Previous analyses revealed that HHM is widely expressed in differentiated cells in adults. Thus, the transcription suppressing activity of HHM may not be controlled by its expression level, but by the dynamic equilibrium between the autoinhibited and relaxed forms. In contrast, the expression of the Id family proteins is robustly regulated, and is induced in response to extracellular signalling molecules, including bone morphogenetic proteins (Miyazono *et al*, 2010). As the Id family proteins are stronger antagonists of the DNA-binding activity of the target transcription factors than HHM (Terai *et al*, 2000), their activities may be principally controlled at the expression level. Consistently, the amino-acid sequences of the Id family proteins suggest that they lack the extra domain that may act as the cradle in HHM.

Mutations that disrupt the interactions between HLH and the N- and C-bundles compromise the transcription factor specificity of HHM

To functionally examine the above hypothesis, we created four HHM mutants designed to weaken the interactions between the HLH and the N- and C-bundles. In the first mutant, Pro166, which is located in the L5 loop connecting helices α5 and α6 (Figure 2D), was mutated to a bulky Tyr (HHM-P166Y) to destabilize the V-shaped conformation. In

©2012 European Molecular Biology Organization

the second mutant, Asn169, which resides at the N terminus of helix α6 and interacts with both the N- and C-bundles (Figure 2C), was mutated to Glu (HHM-N169E) to destabilize the association between α6 and α4/8. Sedimentation velocity experiments were performed to verify that these mutants do not form aggregates (Figure 5C, middle and lower panels). The results also showed that the mutants have sedimentation coefficients of 2.5–2.6 *S*, corresponding to that of the relaxed form of wild-type HHM. Thus, these mutants may originally adopt the relaxed form, as expected. In the third and fourth mutants, Val271 and Val278 on α8 in the C-bundle were mutated to Phe and Arg, respectively (HHM-V271F, HHM-V278R). The expression levels of these mutants in COS7 cells were similar to that of the wild type, suggesting that the overall structure or stability is maintained. We then examined the physical interactions of these mutants with HLH proteins (Olig1, NeuroD1, and Id2) as well as cyclin D1 (Figure 6). The wild-type HHM and all of the mutants almost equally interacted with Olig1 and cyclin D1. In contrast, the wild-type HHM only weakly interacted with NeuroD1 and Id2, while the four mutants more efficiently interacted with these non-cognate HLH proteins. These mutations thus relaxed the binding specificity for HLH transcription factors.

We next examined whether the loss of strict binding specificity in HHM mutants affects cellular process using an *in vitro* cell differentiation system. Myoblastic C2C12 cells undergo myogenic differentiation when they are cultured with a low concentration of serum (Bains *et al*, 1984). The adenoviral constructs bearing HHM or its mutants were used to infect the cells for ectopic expression, followed by induction of differentiation. Myogenic differentiation was assessed by mRNA expression of myosin heavy chain as well as myogenin (Figure 7). At 12 h after the induction of differentiation, marker expression was not significantly different among samples. At 24 h after induction, wild-type HHM did not significantly affect myogenic differentiation compared with empty vector control. In contrast, the P166Y, N169E, V271F, and V278R mutants all enhanced expression of myosin heavy chain and myogenin. Thus,

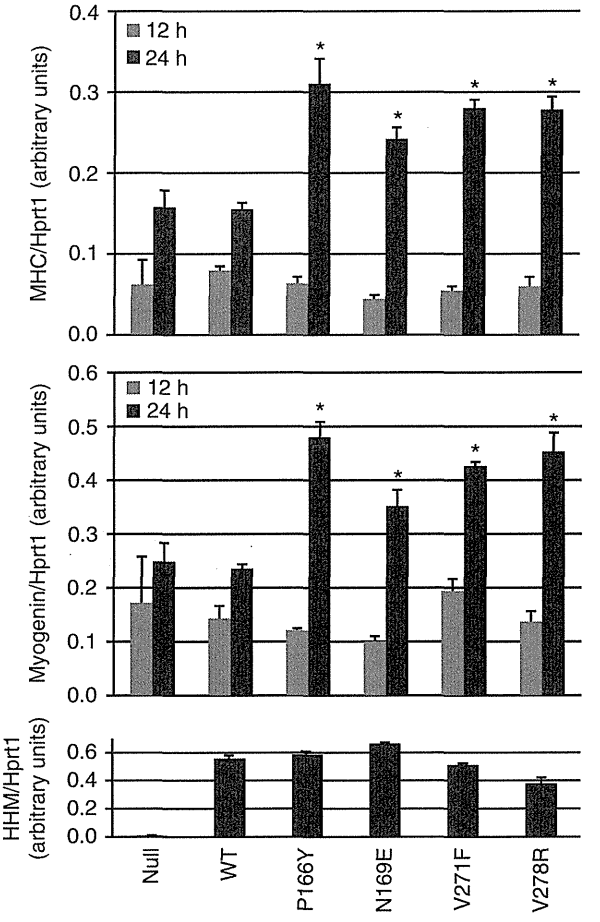

Figure 7 Accelerated myogenic differentiation by HHM mutants. C2C12 cells were infected with adenoviruses carrying empty vector, HHM or its mutants. After 24 h, the cells were cultured in differentiation medium. Twelve or twenty-four hours later, the cells were collected and measured for expression of myogenic markers, myosin heavy chain (MHC), and myogenin. Expression of HHM at 24 h is also shown. Data were normalized by expression of hypoxanthine phosphoribosyltransferase 1. Error bars represent s.d. $^*P<0.01$ compared with both Adeno-null and HHM wild type.

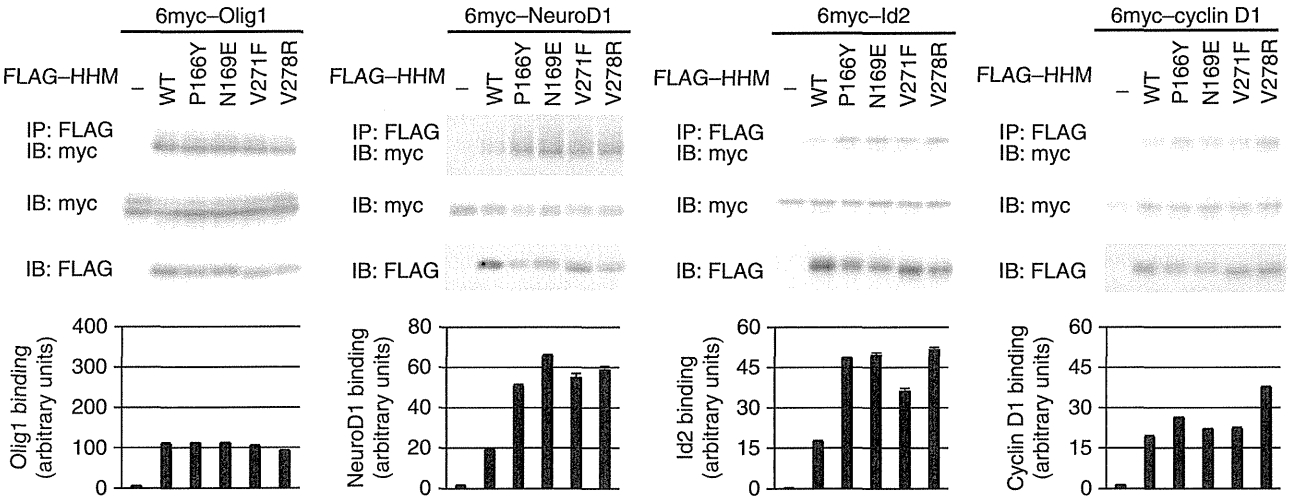

Figure 6 Physical interactions of HHM mutants with HLH proteins and cyclin D1. COS7 cells were transfected with the indicated plasmids (FLAG-tagged HHM or HHM mutants and 6myc-tagged Olig1, NeuroD1, Id2, or cyclin D1). HHM and its mutants were immunoprecipitated (IP), and the co-precipitated proteins were visualized by immunoblotting (top panel). Input of each target protein (second panel), HHM and its mutants (third panel) are also shown. Representative data from three independent experiments are presented. HHM-bound proteins are quantified at the bottom. Error bars represent s.d.

©2012 European Molecular Biology Organization

these HHM mutants appear to accelerate myogenic cell differentiation, possibly by acting as dnHLH proteins with relaxed binding specificity. At present, the precise mode of action remains to be elucidated. Myogenic differentiation is driven by the active complex formation between class-I E12/47 and class-II MyoD (Lassar *et al*, 1991). We observed that HHM and its mutants failed to interact with MyoD (Supplementary Figure S6). In contrast, HHM mutants, but not wild-type HHM, efficiently interacted with Id2 (Figure 6). Id proteins are known to disrupt E12/E47–MyoD complex to inhibit its transcriptional activity (Benezra *et al*, 1990). Thus, the HHM mutants are likely to bind and sequester Ids, which originally suppress the E12/47–MyoD complex, accelerating myogenic differentiation by the reformation of the active complex between E12/47 and MyoD. At 36 h, difference was less clear in expression of myogenin and not evident in expression of myosin heavy chain (data not shown).

Altogether, these findings suggest that the V-shaped conformation of the free-form HHM not only has an autoinhibitory function, but also controls the transcription factor binding activity to enhance the factor specificity.

Concluding remarks

The present structural and functional studies on HHM suggested that the V-shaped form of HHM is the autoinhibited state for transcriptional regulation, and that the dynamic equilibrium between the V-shaped and relaxed forms controls the transcription suppressing activity of HHM (Figure 4B). Thus, HHM appears to play important roles in cellular regulation, including suppression of tumour progression by controlling activities of HLH transcription factors, such as Olig1, through conformational transition. Our present study also highlights the impact of regulation of binding specificities of HLH proteins, to ensure successful coordination of cellular responses mediated by a network of HLH proteins, total understanding of which may explain the patho-physiological processes of dnHLH proteins.

Materials and methods

Sample preparation and crystallization

The selenomethionine-derivatized HHM (SeM-HHM) proteins were prepared as previously described (Seto *et al*, 2009), with slight modifications as follows: (i) the reducing reagent (5 mM β-mercaptoethanol) was replaced by 10 mM *tris*(2-carboxyethyl)phosphine (TCEP), and (ii) the final gel filtration chromatography purification step was omitted. The purified protein sample was treated with PCMB, to prevent the formation of nonspecific intermolecular disulphide bonds. The stoichiometry of the mercury and the sulphydryl groups in the protein monomer was adjusted to 1:1. Subsequently, the PCMB-treated protein solution was concentrated to 10 mg/ml. The crystals of PCMB-treated SeM-HHM were prepared as previously described (Seto *et al*, 2009).

The C198S/C300S mutant of HHM (HHM-CS) was prepared by site-directed mutagenesis using a QuikChange™ Site-Directed Mutagenesis kit (Stratagene), according to the manufacturer's instructions. The HHM-CS protein was also prepared as described above, without the PCMB treatment step. The crystals of HHM-CS were obtained by the sitting-drop vapour diffusion method. The drops were prepared by mixing equal volumes of a 10 mg/ml HHM-CS solution and a reservoir solution, containing 100 mM imidazole (pH 8.0), 500 mM $(NH_4)_2HPO_4$, and 100 mM NaCl. The crystals grew to a size of 0.3 mm × 0.3 mm × 0.5 mm within a week. The crystals were transferred stepwise to the harvesting solution, 200 mM potassium citrate, 10 mM TCEP and 13% (w/v) PEG3350, containing 35% (v/v) xylitol as a cryoprotectant, and were flash-cooled in a nitrogen stream at 100 K.

Data collection, processing, and structure determination

All diffraction data sets were collected at the station NW12A at KEK PF-AR (Tsukuba, Japan). Data sets were processed with the HKL2000 suite (HKL Research). The statistics of the data processing are summarized in Tables I and II. The structure determination of wild-type SeM-HHM by the MAD method was performed as previously described (Seto *et al*, 2009). The phase calculation statistics are summarized in Table I. The resulting initial model was manually modified to fit into the electron density maps by the programs O (Jones *et al*, 1991) and Coot (Emsley and Cowtan, 2004).

The crystals of the HHM-CS mutant belonged to the same space group as the wild-type protein crystals. The structure of the HHM-CS mutant was determined by the molecular replacement method with the program MOLREP (Vagin and Teplyakov, 2000), using the structure of wild-type SeM-HHM as the search model. No significant differences between the wild-type and mutant HHM structures were

Table I Data collection and phasing statistics

Data collection statistics	SeMet (wild type)		
X-ray source	PF-AR NW12A		
Wavelength (Å)	Peak	Edge	Remote
	0.97912	0.97928	0.96405
Space group	$P3_221$		
Unit cell dimensions (Å,°)	$a=b=106.8$, $c=119.5$ $\alpha=\beta=90$, $\gamma=120$		
Resolution (Å)	50–3.1 (3.15–3.1)	50–3.2 (3.26–3.2)	50–3.4 (3.46–3.4)
Unique reflections	14 633 (711)	13 671 (619)	11 593 (485)
Redundancy	15.5 (6.1)	14.7 (4.2)	7.1 (2.7)
Completeness (%)	99.8 (98.1)	99.3 (90.5)	97.9 (83.3)
$I/\sigma(I)$	49.9 (2.48)	43.7 (1.97)	36.9 (1.62)
R_{sym}	0.081 (0.404)	0.069 (0.413)	0.064 (0.416)
Phasing statistics			
No. of Se sites	11		
Phasing power			
Iso (cen./acen.)	0.673/0.783	—	0.182/0.194
Ano	2.580	1.627	0.916
R_{cullis}			
Iso (cen./acen.)	0.797/0.822	—	0.998/1.004
Ano	0.530	0.690	0.862
Mean FOM			
Cen./acen.	0.22/0.40		

The numbers in parentheses are for the last shell.

©2012 European Molecular Biology Organization

Table II Data collection and structure refinement statistics

Data collection statistics	Native (C198S/C300S)
X-ray source	PF-AR NW12A
Wavelength (Å)	1.0
Space group	$P3_221$
Unit cell dimensions (Å,°)	$a=b=105.0$, $c=124.3$, $\alpha=\beta=90$, $\gamma=120$
Resolution (Å)	50–2.5 (2.54–2.5)
Unique reflections	25 654 (1263)
Redundancy	6.8 (3.6)
Completeness (%)	91.8 (91.6)
$I/\sigma(I)$	40.1 (2.46)
R_{sym}	0.046 (0.371)
Refinement statistics	
Resolution (Å)	50–2.5
No. of reflections (all/test)	25 638/1271
R_{work}/R_{free}	0.2220/0.2612
No. of atoms	
Non-hydrogen	2333
Water	52
RMSD of	
Bond length (Å)	0.006
Bond angle (°)	1.029
Average B-factor (Å^2)	99.6
Ramachandran plot	
Most favoured (%)	95.6
Allowed region (%)	4.4
Disallowed region (%)	0

The numbers in parentheses are for the last shell.

observed. Finally, the atomic models of the HHM-CS mutant were refined against reflections up to 2.5 Å resolution, using the program PHENIX (Adams *et al*, 2002). The final round of refinement treated the N-terminal (1–167) and C-terminal (168–360) regions as independent TLS groups, which significantly lowered the value of R_{free}. The structural refinement statistics are summarized in Table II. Molecular graphics were illustrated using CueMol (http://www.cuemol.org/).

GST pull-down assay

Equal amounts of GST-HHM(wt), GST-HHM(TEV), and GST-HHM(TEV) following TEV protease cleavage were incubated with Glutathione Sepharose 4B beads. The beads were washed three times in the binding/washing buffer (50 mM Tris-HCl, pH 8.0, containing 150 mM NaCl, 1 mM EDTA, and 0.1% NP-40). The bound proteins were eluted with the SDS-PAGE sample buffer, resolved by SDS-PAGE, and stained by Coomassie Brilliant Blue.

Analytical ultracentrifugation

Prior to analytical ultracentrifugation, the samples were purified by gel filtration chromatography, in 20 mM Tris-Cl buffer (pH 7.5) containing 200 mM NaCl and 7 mM TCEP. The same buffer was used as the reference solution. Sedimentation velocity experiments were performed with an Optima XL-I analytical ultracentrifuge (Beckman-Coulter). Sample (400 µl) and reference (420 µl) solutions were loaded into double sector centrepieces mounted in a Beckman An-50Ti rotor. The concentration profiles of the samples were monitored by the absorbance at 280 nm, without intervals between successive scans. The data were analysed by the SEDFIT program (Schuck, 2000) to obtain the $c(s)$ profiles. On the basis of the assumption that the frictional ratio f/f_0 was common to all of the molecular species, $c(s)$ was converted to obtain the molecular mass distribution function, $c(M)$, using the implemented function in SEDFIT. The partial specific volume ($\bar{v}$) of HHM from the amino-acid sequence, the buffer density (ρ), and viscosity (η), based on the solvent composition, were calculated by the SEDNTERP program (Laue *et al*, 1992).

Sedimentation equilibrium experiments were carried out in an Optima XL-I analytical ultracentrifuge, using a 4-hole An60Ti rotor at 20 °C with a standard double sector centrepieces and quartz windows. A quantity of 120 µl of each sample with the absorption of 0.2, 0.3, and 0.5 at 280 nm was applied in the sample hole, and the corresponding dialysate was loaded in the reference hole of the cell. The concentration gradients of the samples were monitored by absorption at 280 nm. The rotor speeds were 8800 r.p.m. for 24 h, 12 600 r.p.m. for 20 h, and 22 000 r.p.m. for 20 h. Scans were made every 2 h, and the equilibrium of the system was assumed when the last three scans were identical. Totally, nine data sets were globally fitted to a single species model to determine the weight-average-molecular weight by the nonlinear least-square fitting, as implemented in the Beckman-Coulter software package.

Protein binding assay

The expression constructs encoding HHM, human Olig1, and human Id2 were described previously (Ikushima *et al*, 2008). The full-length cDNA encoding mouse NeuroD1 was synthesized and cloned into the mammalian expression vector pcDNA3. The cDNAs encoding HHM mutants were generated using a PCR-based approach. COS7 cells were obtained from the American Type Culture Collection, and were maintained in Dulbecco's modified Eagle's medium (DMEM) containing 10% fetal bovine serum (FBS), 50 U/ml penicillin, and 50 µg/ml streptomycin. Cells were transfected with various plasmids, using the FuGENE6 transfection reagent (Roche Diagnostics) according to the manufacturer's recommendations. Cell lysis, immunoprecipitation, and immunoblotting were performed as described previously (Mizutani *et al*, 2010). An anti-FLAG M2 antibody (Sigma-Aldrich) and an anti-Myc 9E10 antibody (Pharmingen) were used for immunological detection of proteins. Immunoblotting images were obtained using a Luminescent Image Analyzer (LAS-4000, Fujifilm). Bands on immunoblots were quantified using the Image-J software (National Institutes of Health, USA). All luminescent images were acquired and quantified under unsaturated conditions.

Myogenic differentiation assay

cDNAs encoding HHM and its mutants were cloned into a modified pENTR vector (Invitrogen) carrying CAG promoter and polyA signal (excised from pAxCAwt, Takara Bio), and introduced into the adenoviral genome via recombination between pENTR vector and the pAd/PL/DEST vector using LR Clonase (Invitrogen). HEK293A cells were transfected with pAd/PL/HHM after linearization of it with PacI. Viral particles were isolated by three freeze-thaw cycles and amplified by reinfection in HEK293A cells. C2C12 cells were obtained from the American Type Culture Collection, and were maintained in DMEM containing 20% FBS, 50 U/ml penicillin, and 50 µg/ml streptomycin. C2C12 cells were plated on a six-well culture dish (5×10^4 cells/well), infected with adenoviruses, and cultured for 24 h. The cells were then cultured in differentiation medium (DMEM containing 2% FBS) for 12–24 h. Myogenic marker expression was determined by quantitative real-time PCR analysis as described previously (Koinuma *et al*, 2011). Primer sequences used are as follows: mouse *myosin heavy chain* (sense, 5′- CCGG TGCTGTGATGCATTATG-3′; antisense, 5′-CAGCAACTTCGGTGC CATCT-3′); mouse *myogenin* (sense, 5′-CCAGGAGATCATTTGCTC GC-3′; antisense, 5′-TGATGCTGTCCACGATGGAC-3′); HHM (sense, 5′-GCAGTCCCCACCCTGGCTTC-3′; antisense, 5′-GAGCAACCGCAGC TCCTCCG-3′); mouse hypoxanthine phoshoribosyltransferase 1 (sense, 5′-CAGGCCAGACTTTGTTGGAT-3′; antisense, 5′-AACTTG CGCTCATCTTAGGC-3′).

Multiple comparisons of the data were performed using the Tukey–Kramer method.

Accession codes

The atomic coordinates have been deposited in the Protein Data Bank under accession code 3AY5.

Supplementary data

Supplementary data are available at *The EMBO Journal* Online (http://www.embojournal.org).

©2012 European Molecular Biology Organization

Acknowledgements

We are grateful to Dr Nakamura (University of Tokyo) for helpful discussions regarding the construction of the atomic model of HHM. We thank the beam-line staffs at BL41XU of SPring-8 and NW12A of KEK PF-AR for assistance in data collection. We thank the RIKEN Integrated Cluster of Clusters (RICC) for providing computational resources. This work was supported by a grant from the Japan Society for the Promotion of Science (JSPS) through its 'Funding Program for World-Leading Innovative R&D on Science and Technology (FIRST program)' to ON, by Core Research for Evolutional Science and Technology (CREST) Program 'The Creation of Basic Medical Technologies to Clarify and Control the Mechanisms Underlying Chronic Inflammation' of Japan Science and Technology Agency (JST) to ON, by a Grant-in-Aid for Scientific Research on Innovative Areas from MEXT to KoM, RI, and ON, by the Kurata Memorial Hitachi Science and Technology Foundation grant to ON, and by a grant from the Fugaku Memorial Foundation and the Mitsubishi Science Foundation to KeM.

Author contributions: Ryohei Ishii, Daizo Koinuma, Kohei Miyazono, Keiji Miyazawa, Ryuichiro Ishitani, and Osamu Nureki designed the experiments and analysed the data; Ryohei Ishii, Kazunobu Isogaya, Azusa Seto, Daizo Koinuma, Yuji Watanabe, So-ichi Yaguchi, Hiroaki Ikushima, Naoshi Dohmae, Ryuichiro Ishitani, and Osamu Nureki performed the most experiments; Fumio Arisaka designed and performed the analytical ultracentrifugation experiments; Ryohei Ishii, Daizo Koinuma, Keiji Miyazawa, Ryuichiro Ishitani, and Osamu Nureki wrote the paper; Keiji Miyazawa and Osamu Nureki supervised the project.

Conflict of interest

The authors declare that they have no conflict of interest.

References

Adams PD, Grosse-Kunstleve RW, Hung LW, Ioerger TR, McCoy AJ, Moriarty NW, Read RJ, Sacchettini JC, Sauter NK, Terwilliger TC (2002) PHENIX: building new software for automated crystallographic structure determination. *Acta Crystallogr* D58: 1948–1954

Ayer DE, Kretzner L, Eisenman RN (1993) MAD—a heterodimeric partner for max that antagonizes Myc transcriptional activity. *Cell* **72:** 211–222

Bains W, Ponte P, Blau H, Kedes L (1984) Cardiac actin is the major actin gene-product in skeletal-muscle cell-differentiation *in vitro*. *Mol Cell Biol* **4:** 1449–1453

Benezra R, Davis RL, Lockshon D, Turner DL, Weintraub H (1990) The protein Id—A negative regulator of helix-loop-helix DNA-binding proteins. *Cell* **61:** 49–59

Blackwell TK, Kretzner L, Blackwood EM, Eisenman RN, Weintraub H (1990) Sequence-specific DNA-binding by the C-Myc protein. *Science* **250:** 1149–1151

Blackwood EM, Eisenman RN (1991) Max—a helix-loop-helix zipper protein that forms a sequence-specific DNA-binding complex with myc. *Science* **251:** 1211–1217

Chavali GB, Vijayalakshmi C, Salunke DM (2001) Analysis of sequence signature defining functional specificity and structural stability in helix-loop-helix proteins. *Proteins* **42:** 471–480

Crews ST (1998) Control of cell lineage-specific development and transcription by bHLH-PAS proteins. *Genes Dev* **12:** 607–620

de la Torre JG, Huertas ML, Carrasco B (2000) Calculation of hydrodynamic properties of globular proteins from their atomic-level structure. *Biophys J* **78:** 719–730

Emsley P, Cowtan K (2004) Coot: model-building tools for molecular graphics. *Acta Crystallogr Sect D-Biol Crystallogr* **60:** 2126–2132

Fong S, Debs RJ, Desprez PY (2004) Id genes and proteins as promising targets in cancer therapy. *Trends Mol Med* **10:** 387–392

Han SA, Guo CC, Hong L, Liu H, Zheyi H, Liu CJ, Wang J, Wu KC, Ding J, Fan DM (2004) Expression and significance of Id1 helix-loop-helix protein overexpression in gastric cancer. *Cancer Lett* **216:** 63–71

Hwang SY, Oh B, Fuchtbauer A, Fuchtbauer EM, Johnson KR, Solter D, Knowles BB (1997) Maid: a maternally transcribed novel gene encoding a potential negative regulator of bHLH proteins in the mouse egg and zygote. *Dev Dyn* **209:** 217–226

Ikushima H, Komuro A, Isogaya K, Shinozaki M, Hellman U, Miyazawa K, Miyazono K (2008) An Id-like molecule, HHM, is a synexpression group-restricted regulator of TGF-beta signalling. *EMBO J* **27:** 2955–2965

Ishiguro A, Spirin K, Shiohara M, Tobler A, Norton JD, Rigolet M, Shimbo T, Koeffler HP (1995) Expression of Id2 and Id3 mRNA in human lymphocytes. *Leuk Res* **19:** 989–996

Jones TA, Zou JY, Cowan SW, Kjeldgaard M (1991) Improved methods for building protein models in electron-density maps and the location of errors in these models. *Acta Crystallogr Sect A* **47:** 110–119

Klambt C, Knust E, Tietze K, Camposortega JA (1989) Closely related transcripts encoded by the neurogenic gene-complex enhancer of split of *Drosophila melanogaster*. *EMBO J* **8:** 203–210

Koinuma D, Shinozaki M, Nagano Y, Ikushima H, Horiguchi K, Goto K, Chano T, Saitoh M, Imamura T, Miyazono K, Miyazawa K (2011) RB1CC1 protein positively regulates transforming growth factor-β signaling through the modulation of Arkadia E3 ubiquitin ligase activity. *J Biol Chem* **286:** 32502–32532

Kreider BL, Benezra R, Rovera G, Kadesch T (1992) Inhibition of myeloid differentiation by the helix-loop-helix protein Id. *Science* **255:** 1700–1702

Lassar AB, Davis RL, Wright WE, Kadesch T, Murre C, Voronova A, Baltimore D, Weintraub H (1991) Functional-activity of myogenic hlh proteins requires hetero-oligomerization with E12/E47-Like proteins *in vivo*. *Cell* **66:** 305–315

Laue TM, Shah BD, Ridgeway TM, Pelletier SL (1992) Computer-aided interpretation of analytical sedimentation data for proteins. In *Analytical Ultracentrifugation in Biochemistry and Polymer Science*, Harding SE, Rowe AJ, Horton JC (eds) pp 90–125. Cambridge, UK: Royal Society of Chemistry

Lee JE, Hollenberg SM, Snider L, Turner DL, Lipnick N, Weintraub H (1995) Conversion of xenopus ectoderm into neurons by neurod, a basic helix-loop-helix protein. *Science* **268:** 836–844

Longo A, Guanga GP, Rose RB (2008) Crystal structure of E47-NeuroD1/beta2 bHLH domain-DNA complex: heterodimer selectivity and DNA recognition. *Biochemistry* **47:** 218–229

Ma QF, Kintner C, Anderson DJ (1996) Identification of neurogenin, a vertebrate neuronal determination gene. *Cell* **87:** 43–52

Ma W, Xia X, Stafford LJ, Yu C, Wang F, LeSage G, Liu M (2006) Expression of GCIP in transgenic mice decreases susceptibility to chemical hepatocarcinogenesis. *Oncogene* **25:** 4207–4216

Massari ME, Murre C (2000) Helix-loop-helix proteins: regulators of transcription in eucaryotic organisms. *Mol Cell Biol* **20:** 429–440

Miyazono K, Kamiya Y, Morikawa M (2010) Bone morphogenetic protein receptors and signal transduction. *J Biochem* **147:** 35–51

Mizutani A, Saitoh M, Imamura T, Miyazawa K, Miyazono K (2010) Arkadia complexes with clathrin adaptor AP2 and regulates EGF signalling. *J Biochem* **148:** 733–741

Murre C, McCaw PS, Vaessin H, Caudy M, Jan LY, Jan YN, Cabrera CV, Buskin JN, Hauschka SD, Lassar AB, Weintraub H, Baltimore D (1989) Interactions between heterologous helix-loop-helix proteins generate complexes that bind specifically to a common DNA-sequence. *Cell* **58:** 537–544

Nair SK, Burley SK (2003) X-ray structures of Myc-Max and Mad-Max recognizing DNA: Molecular bases of regulation by proto-oncogenic transcription factors. *Cell* **112:** 193–205

Olson EN, Klein WH (1994) bHLH factors in muscle development—dead lines and commitments, what to leave in and what to leave out. *Genes Dev* **8:** 1–8

Parkhurst SM, Meneely PM (1994) Sex determination and dosage compensation—lessons from flies and worms. *Science* **264:** 924–932

Perk J, Iavarone A, Benezra R (2005) ID family of helix-loop-helix proteins in cancer. *Nat Rev Cancer* **5:** 603–614

Rawls A, Olson EN (1997) MyoD meets its maker. *Cell* **89:** 5–8

Rushlow CA, Hogan A, Pinchin SM, Howe KM, Lardelli M, Ishhorowicz D (1989) The *Drosophila* hairy protein acts in both

©2012 European Molecular Biology Organization

segmentation and bristle patterning and shows homology to N-MYC. *EMBO J* **8:** 3095–3103

Schuck P (2000) Size-distribution analysis of macromolecules by sedimentation velocity ultracentrifugation and Lamm equation modeling. *Biophys J* **78:** 1606–1619

Seto A, Ikushima H, Suzuki T, Sato Y, Fukai S, Yuki K, Miyazawa K, Miyazono K, Ishitani R, Nureki O (2009) Crystallization and preliminary X-ray diffraction analysis of GCIP/HHM transcriptional regulator. *Acta Crystallogr F-Struct Biol Cryst Commun* **65:** 21–24

Shen CP, Kadesch T (1995) B-cell-specific DNA-binding by an E47 homodimer. *Mol Cell Biol* **15:** 4518–4524

Sonnenberg-Riethmacher E, Wustefeld T, Miehe M, Trautwein C, Riethmacher D (2007) Maid (GCIP) is involved in cell cycle control of hepatocytes. *Hepatology* **45:** 404–411

Sun XH, Copeland NG, Jenkins NA, Baltimore D (1991) ID proteins ID1 and ID2 selectively inhibit DNA-binding by one class of helix-loop-helix proteins. *Mol Cell Biol* **11:** 5603–5611

Terai S, Aoki H, Ashida K, Thorgeirsson SS (2000) Human homologue of maid: a dominant inhibitory helix-loop-helix protein associated with liver-specific gene expression. *Hepatology* **32:** 357–366

Vagin A, Teplyakov A (2000) An approach to multi-copy search in molecular replacement. *Acta Crystallogr Sect D-Biol Crystallogr* **56:** 1622–1624

Wang Q, Tsao SW, Fu SB, Xue WC, Meng XN, Feng HC, Wong YC, Wang XH (2004) Overexpression of Id-1 in gastric adenocarcinoma: implication for a novel diagnostic marker. *Anticancer Res* **24:** 881–886

Weintraub H (1993) The MyoD family and myogenesis—redundancy, networks, and thresholds. *Cell* **75:** 1241–1244

Weintraub H, Davis R, Lockshon D, Lassar A (1990) MyoD binds cooperatively to 2 sites in a target enhancer sequence—occupancy of 2 sites is required for activation. *Proc Natl Acad Sci USA* **87:** 5623–5627

Weintraub H, Dwarki VJ, Verma I, Davis R, Hollenberg S, Snider L, Lassar A, Tapscott SJ (1991) Muscle-specific transcriptional activation by MyoD. *Genes Dev* **5:** 1377–1386

Wibley J, Deed R, Jasiok M, Douglas K, Norton J (1996) A homology model of the Id-3 helix-loop-helix domain as a basis for structure-function predictions. *Biochim Biophys Acta-Protein Struct Molec Enzym* **1294:** 138–146

Xia CZ, Bao ZM, Tabassam F, Ma WB, Qiu MS, Hua SB, Liu MY (2000) GCIP, a novel human Grap2 and cyclin D interacting protein, regulates E2F-mediated transcriptional activity. *J Biol Chem* **275:** 20942–20948

Yokota Y, Mori S (2002) Role of id family proteins in growth control. *J Cell Physiol* **190:** 21–28

Zebedee Z, Hara E (2001) Id proteins in cell cycle control and cellular senescence. *Oncogene* **20:** 8317–8325

Zervos AS, Gyuris J, Brent R (1993) MXI1, a protein that specifically interacts with max to bind Myc-Max recognition sites. *Cell* **72:** 223–232

 ©2012 European Molecular Biology Organization

Original Article

Extended Field Stereotactic Radiosurgery for Recurrent Glioblastoma

Tomoyuki Koga, MD[1]; Keisuke Maruyama, MD, PhD[1]; Minoru Tanaka, MD, PhD[1]; Yasushi Ino, MD, PhD[1,2]; Nobuhito Saito, MD, PhD[1]; Keiichi Nakagawa, MD, PhD[3]; Junji Shibahara, MD, PhD[4]; and Tomoki Todo, MD, PhD[1,2]

BACKGROUND: Stereotactic radiosurgery (SRS) is among the few therapeutic options for glioblastoma that recurs after standard radiation and chemotherapy, but its efficacy has been limited. **METHODS:** Since November 2007, the authors have modified the clinical target volume by adding a 0.5- to 1-cm margin to the gadolinium-enhanced area (extended field SRS), in contrast to conventional SRS using no margin to set the clinical target volume. A total of 35 recurred glioblastoma lesions in 9 patients were treated with conventional SRS between December 1990 and January 2007, and 14 lesions in 9 patients were treated with extended field SRS. **RESULTS:** The median follow-up periods were 7 months (range, 3-29 months) and 8 months (range, 6-27 months), respectively. The local control rate was 47% for conventional SRS and 93% for extended field SRS ($P = .0035$), and the numbers of radiation necrosis observed in SRS-treated lesions were 2 and 4, respectively. The median overall survival from the diagnosis was 24 months (range, 14-57 months) for conventional SRS and 21 months (range, 15-51 months) for extended field SRS (statistically not significant). Seven patients treated with conventional SRS died during follow-up, 6 from progression of the SRS-treated tumor, whereas 7 patients treated with extended field SRS died during follow-up, 6 from remote intracerebral dissemination. **CONCLUSIONS:** Extended field SRS was superior to conventional SRS in the local control of small recurrent lesions of glioblastoma, although a further device to suppress remote dissemination may be necessary to increase survival. ***Cancer* 2012;118:4193-200.** © *2011 American Cancer Society.*

KEYWORDS: glioblastoma, glioma, gamma knife, stereotactic radiosurgery, radiation therapy, recurrence.

INTRODUCTION

Glioblastoma is a highly malignant and aggressive tumor of the central nervous system that corresponds to grade IV of the World Health Organization histological classification.[1] The current standard treatment for glioblastoma is a maximal resection with functional preservation, followed by radiation and chemotherapy. When temozolomide is used for chemotherapy, the median survival is 14.6 months after initial presentation,[2] and ranges from 5 to 13 months after recurrence.[3,4] Because of the aggressive and invasive nature of the tumor, recurrence is seen in >90% of patients.[5] The most common pattern of recurrence is local regrowth[6]; therefore, successful local control should lead to prolongation of patients' survival. Various local treatment strategies have been attempted, including repeated operations, conformal radiotherapy, brachytherapy, and local chemotherapy.[7]

Although stereotactic radiosurgery (SRS) is an option as salvage treatment for recurrent glioblastoma in clinical settings, the role of SRS is still limited for glioma. SRS is useful in controlling relatively well-demarcated glioma such as ependymoma, pilocytic astrocytoma, and pleomorphic xanthoastrocytoma.[8-13] However, the majority of glioma is infiltrative to brain parenchyma and is difficult to target with SRS. A randomized controlled study proved that there was no benefit in upfront SRS before conventional fractionated radiation therapy for patients with glioblastoma.[14] Several reports indicate the usefulness of adjuvant SRS at recurrence for glioblastoma, median survival time after SRS being 4.6 to 16 months,[15-20] although a randomized study is needed to prove efficacy. The major cause of treatment failure in managing recurrent glioblastoma by SRS is assumed to be that the highly conformal irradiation spares the surrounding tissue, which is presumably infiltrated with viable tumor cells.[21-23] With the intent to cover such tissue surrounding the bulk of tumor as much as possible, we changed the treatment protocol of SRS for recurrent glioblastoma lesions by extending the clinical target volume.[24] We present the early results of this newly applied treatment strategy.

Corresponding author: Tomoki Todo, MD, PhD, Division of Innovative Cancer Therapy, Institute of Medical Science, University of Tokyo, 4-6-1 Shirokanedai, Minato-ku, Tokyo 108-8639 Japan; Fax: (011) + 81-3-6409-2147; toudou-nsu@umin.ac.jp

[1]Department of Neurosurgery, University of Tokyo Hospital, Tokyo, Japan; [2]Translational Research Center, University of Tokyo Hospital, Tokyo, Japan; [3]Department of Radiology, University of Tokyo Hospital, Tokyo, Japan; [4]Department of Pathology, University of Tokyo Hospital, Tokyo, Japan

DOI: 10.1002/cncr.27372, **Received:** June 12, 2011; **Revised:** September 19, 2011; **Accepted:** October 24, 2011, **Published online** December 16, 2011 in Wiley Online Library (wileyonlinelibrary.com)

Table 1. Characteristics of the Patients Who Received Conventional SRS

Case No.	Age, y/Sex	Initial Hx	Initial Tx	Time from Dx to 1st SRS, mo	No. of Lesions	Controlled Lesions	Time to Local Relapse, mo	Last F/U, mo after 1st SRS	Outcome
1	25/M	Glioblastoma	EBRT, ACNU	22	3	1/3	4	4	Lost to F/U
2	40/M	Glioblastoma	EBRT, ACNU	17	1	0/1	9	29	Dead
3	43/M	Glioblastoma	EBRT, ACNU	10	3	0/3	10	16	Dead
4	62/M	AA	EBRT, ACNU	1	1	NA	NA	13	Dead
5	43/M	Glioblastoma	EBRT, ACNU	6	5	3/5	7	8	Lost to F/U
6	59/F	Glioblastoma	EBRT, CE	15	6	1/6	6	7	Dead
7	17/F	Glioblastoma	BNCT, TMZ	14	6	5/6	6	6	Dead
8	64/F	Glioblastoma	EBRT, ACNU	19	1	0/1	1	3	Dead
9	54/M	Glioblastoma	EBRT, TMZ	51	9	6/9	5	6	Dead

Abbreviations: AA, anaplastic astrocytoma; ACNU, nimustine hydrochloride; BNCT, boron neutron capture therapy; CE, carboplatin and etoposide; Dx, diagnosis of glioblastoma; EBRT, external beam radiotherapy; F, female; F/U, follow-up; Hx, histology; M, male; NA, data not available; SRS, stereotactic radiosurgery; TMZ, temozolomide; Tx, treatment.

Table 2. Characteristics of the Patients Who Received Extended Field SRS

Case No.	Age/Sex	Primary Hx	Primary Tx	Time from Dx to 1st SRS, mo	No. of Lesions	Controlled Lesions	Time to Local Relapse, mo	Last F/U, mo after 1st SRS	Outcome
1	53/M	Glioblastoma	EBRT, TMZ	17	1	1/1	—	27	Dead
2	27/M	Glioblastoma	EBRT, TMZ	39	1	0/1	1	12	Dead
3	43/M	AA	EBRT, TMZ	18	1	1/1	—	8	Dead
4	63/M	Glioblastoma	EBRT, TMZ	13	1	1/1	—	10	Dead
5	36/M	DA	EBRT, TMZ	9	3	3/3	—	8	Dead
6	66/F	Glioblastoma	EBRT, TMZ	9	3	3/3	—	6	Dead
7	47/M	Glioblastoma	EBRT, TMZ	12	2	2/2	—	7	Dead
8	58/F	Glioblastoma	EBRT, TMZ	6	1	1/1	—	12	Alive
9	79/F	Glioblastoma	EBRT, TMZ	9	1	1/1	—	8	Alive

Abbreviations: AA, anaplastic astrocytoma; DA, diffuse astrocytoma; Dx, diagnosis of glioblastoma; EBRT, external beam radiotherapy; F, female; F/U, follow-up; Hx, histology; M, male; SRS, stereotactic radiosurgery; TMZ, temozolomide; Tx, treatment.

MATERIALS AND METHODS

Patient Population

Nine patients with recurrent glioblastoma underwent 14 sessions of conventional SRS for 35 lesions using the Leksell Gamma Knife at our institute between December 1990 and January 2007 (Table 1). The median patient age was 43 years (range, 17-64 years). The median Karnofsky Performance Scale score at the first presentation was 90% (range, 80%-90%), and the median Karnofsky Performance Scale score at the time of first SRS for recurrence was 90% (range, 40%-90%). All the patients underwent surgical resection followed by radiation and chemotherapy at the primary onset. Primary lesions were histologically diagnosed as glioblastoma in 8 patients. In 1 patient, the primary lesion was diagnosed as anaplastic astrocytoma, but the recurred lesion was histologically confirmed as glioblastoma after resection. As primary treatment, external beam radiotherapy was applied for 8 patients with the median total dose of 60 grays (Gy; range, 48-80 Gy). Twenty-five of the 35 treated lesions (71%) were within the clinical target volume of the preceding radiotherapy. One patient underwent boron neutron capture therapy. For adjuvant chemotherapy, nimustine hydrochloride was used for 7 patients, carboplatin and etoposide for 1 patient, and temozolomide for 1 patient. The median interval between the time of diagnosis as glioblastoma and the recurrence was 14.5 months (range, 1-51 months).

Nine patients with recurrent glioblastoma underwent 11 sessions of extended field SRS for 14 lesions from November 2007 to April 2010 (Table 2). The extended field SRS was applied to a single recurrent lesion or 2 separate lesions that were $\leq$20 mm in diameter. The median age of this patient group was 53 years (range, 27-79 years). The median Karnofsky Performance Scale score at the first presentation was 90% (range, 80%-90%), and the median Karnofsky Performance Scale score at the time of first SRS for recurrence was 70% (range, 40%-90%).

Seven of these 9 patients underwent surgical resection, and 2 patients received stereotactic biopsy. The initial histological diagnosis was glioblastoma in 7 patients, anaplastic astrocytoma in 1 patient, and diffuse astrocytoma in 1 patient. In the latter 2 patients, lesions were histologically confirmed as glioblastoma at the time of recurrence. All of the 9 patients underwent external beam radiation therapy, with the median total dose of 70 Gy (range, 60-80 Gy). Ten of 14 treated lesions (71%) were within the clinical target volume of the preceding radiotherapy. Seven of them were treated with concomitant and adjuvant temozolomide therapy until the time of SRS for recurrences. For 1 patient, temozolomide was discontinued at the third cycle and nimustine hydrochloride administration was started, because of eruption and thrombocytopenia caused by temozolomide. The other patient received nimustine hydrochloride during radiation, and adjuvant temozolomide therapy was applied for up to 21 cycles until he denied the continuation of the chemotherapy. The median interval between the time of diagnosis as glioblastoma and the recurrence was 12 months (range, 6-39 months).

Conventional SRS

After their heads had been immobilized in the Leksell stereotactic head frame, the patients underwent stereotactic magnetic resonance imaging (MRI) to obtain precise information on the shape, volume, and 3-dimensional coordinates of the tumors. Image-integrated treatment planning was performed jointly by neurosurgeons and radiation oncologists with commercially available software (Leksell GammaPlan; Elekta Instruments AB, Stockholm, Sweden). The clinical target volume was defined as the gadolinium-enhanced lesion without any margin. In principle, the desired dose applied to the margin of each gadolinium-enhanced lesion was 20 Gy. The prescription dose was occasionally reduced because of the tumor volume, the location of lesions, and/or the clinical status of the patient. The median clinical target volume of conventional SRS was 15 cm^3 (range, 3-47 cm^3).

Extended Field SRS

The methods of head fixation, obtaining stereotactic images, and treatment planning and the principle for dose prescription were the same as conventional SRS. The difference was the definition of the clinical target volume, which was extended by adding a 0.5- to 1-cm margin to the periphery of the gadolinium-enhanced lesion. Margin was extended up to a maximum of 1 cm in all directions. By using a dose-volume histogram, the volume that received >20 Gy was determined not to exceed 15 cm^3. The clinical target volume exceeded 15 cm^3 in 2 cases, but the lesions in these patients faced the resection cavity or the ventricle, so the volume of the brain parenchyma included in the clinical target volume was <15 cm^3 in both cases. The median clinical target volume of extended field SRS was 13 cm^3 (range, 6-19 cm^3).

Patient Follow-Up and Statistical Analysis

After SRS, follow-up clinical examinations were performed at our hospital or elsewhere by referring physicians. MRI or computed tomography scanning was taken at 1- to 3-month intervals. When a contrast-enhanced lesion continued to grow at follow-up examinations, it was defined as local control failure unless it was histologically confirmed as radiation necrosis. Conversely, if a contrast-enhanced area ceased to expand or decreased in size during the follow-up with or without the use of steroids, the lesion was recognized as radiation necrosis. Statistical analyses were performed using JMP 8 (SAS Institute, Cary, NC). Fisher exact test was performed to evaluate the significance of differences between conventional SRS and extended field SRS regarding the local control rate and the incidence of radiation necrosis, and the correlation between radiation necrosis and the location of treated lesions. The progression-free and overall survival times were calculated using the Kaplan-Meier method. Factors potentially affecting the survival time were evaluated by log-rank test for univariate analysis.

Ethical Issues

The conduct of this study was approved by our institutional review board. All patients provided written informed consent.

RESULTS

Outcomes of Conventional SRS

Characteristics and outcomes of the patients who underwent conventional SRS are summarized in Table 1. Nine patients who underwent SRS targeting gadolinium-enhanced lesions were followed for the median period of 7 months (range, 3-29 months). Among 34 lesions that could be radiographically followed up, 16 lesions (47%) showed <25% increase of the target area or decreased in size in response to SRS until the last follow-up. All patients who died after conventional SRS possessed uncontrolled SRS-treated lesions. The median time to local relapse after SRS was 6 months (range, 1-10 months). The median survival time after the first SRS for recurrences was 10.5 months (range, 3-29 months). The median overall survival time after the diagnosis of glioblastoma was 24 months (range, 14-57 months), and the

6-month overall survival rate was 63%. As for SRS-induced adverse effects, asymptomatic, radiographically confirmed radiation necrosis was observed in 2 lesions in 2 patients (6.5%). Among these 2 lesions, 1 lesion occurred within the clinical target volume of prior radiotherapy and 1 outside ($P = .59$).

Outcomes of Extended Field SRS

Characteristics and outcomes of the patients who underwent extended field SRS are summarized in Table 2. Nine patients who underwent extended field SRS were followed for the median period of 8 months (range, 5-27 months). Thirteen among 14 lesions (93%) showed <25% increase of the target area or decreased in size in response to SRS until the last follow-up. This local control rate was significantly higher than that of conventional SRS ($P = .0035$). The local relapse in the 1 patient (case 2 in Table 2) was histologically confirmed. Whereas the lesions treated by SRS in 8 patients were controlled until the last follow-up, remote recurrences were observed in 5 patients. Two patients (cases 5 and 6 in Table 2) underwent second SRS for those remote lesions. Another patient (case 3 in Table 2) showed a remote recurrence in the brainstem, for which external beam radiotherapy was performed. The median survival time after the first SRS for recurrences was 9 months (range, 6-27 months), and the 6-month overall survival rate was 89%. There was no statistical difference in survival time after SRS between conventional and extended field SRS ($P = .83$). The median overall survival time after the diagnosis of glioblastoma was 21 months (range, 15-51 months), not statistically different from conventional SRS ($P = .71$). Radiation necrosis was observed in 4 lesions in 4 patients (29%), age ranging from 27 to 53 years, and the frequency was not significantly different from conventional SRS ($P = .052$). The irradiated fields for SRS in these 4 patients all involved the irradiated fields of prior radiotherapy, although this was not statistically significant ($P = .25$). All 4 patients required oral administration of prednisolone at doses of 20 to 30 mg (median, 30 mg) for 7 to 25 months (median, 9 months). As for steroid-related toxicities, moon face and central obesity were observed in all 4 patients, and 1 patient experienced urinary tract infection. By the use of oral steroids, radiation necroses became stable and did not cause deterioration of neurological symptoms in any patients. Karnofsky Performance Scale scores of these 4 patients at the time of first SRS were 90%, 70%, 40%, and 70%. Karnofsky Performance Scale score gradually declined in all 4 patients, mainly because of disseminated lesions, and became 70%, 60%, 40%, and 40% at 6 months after first SRS. The 4 patients died of tumor progression at 27, 12, 8, and 14 months after first SRS. Comparison of patient characteristics and treatment outcomes between conventional and extended field SRS is summarized in Table 3.

Table 3. Comparison of Characteristics and Outcomes of the Patients Who Received Conventional SRS and Extended Field SRS

Characteristic	Conventional SRS	Extended Field SRS	*P*
Number of patients	9	9	—
Primary glioblastoma	8	7	1.0
Patient age, median y, range	43, 17-64	53, 27-79	.36
KPS at onset, median, range	90, 80-90	90, 80-90	.62
Time from Dx to 1st SRS, median mo, range	14.5, 1-51	12, 6-39	.66
KPS at 1st SRS, median, range	90, 40-90	70, 40-90	.21
Local control	16/34	13/14	.0035
Radiation necrosis	2/34	4/14	.052
Median OS after Dx, mo	24	21	.71
Median OS after 1st SRS, mo	10.5	9	.83
6-month OS after 1st SRS, %	63	89	.83

Abbreviations: Dx, diagnosis of glioblastoma; KPS, Karnofsky Performance Scale; OS, overall survival; SRS, stereotactic radiosurgery.

Illustrative Cases

A 17-year-old girl (case 7 in Table 1) presented with right hemiparesis. MRI showed a heterogeneously enhanced mass lesion in the left frontal lobe (Fig. 1A). The tumor was subtotally removed and histologically diagnosed as glioblastoma. Boron neutron capture therapy was performed, and temozolomide was administered orally at a dose of 200 mg/m^2 using the 5 of 28-day regimen. Twelve months after the onset, a diffuse recurrence was observed in the left frontal lobe and the corpus callosum, so she received 50-Gy external beam radiotherapy in 25 fractions. At 14 months, a recurrent lesion 7 mm in diameter was noted in the right frontal lobe, and it was treated by conventional SRS targeting the gadolinium-enhanced lesion with a maximum dose of 40 Gy and a margin dose of 20 Gy (Fig. 1B). However, this lesion continued to grow at 1 month (Fig. 1C) and 3 months (Fig. 1D) after the SRS, and the patient died of diffuse dissemination at 3 months after the SRS.

A 53-year-old man (case 1 in Table 2) presented with left hemiparesis. MRI showed a homogeneously enhanced, poorly circumscribed mass lesion in the right frontal lobe (Fig. 2A). The tumor was subtotally removed and histologically diagnosed as glioblastoma. He received 80-Gy external beam radiotherapy in 40 fractions, with

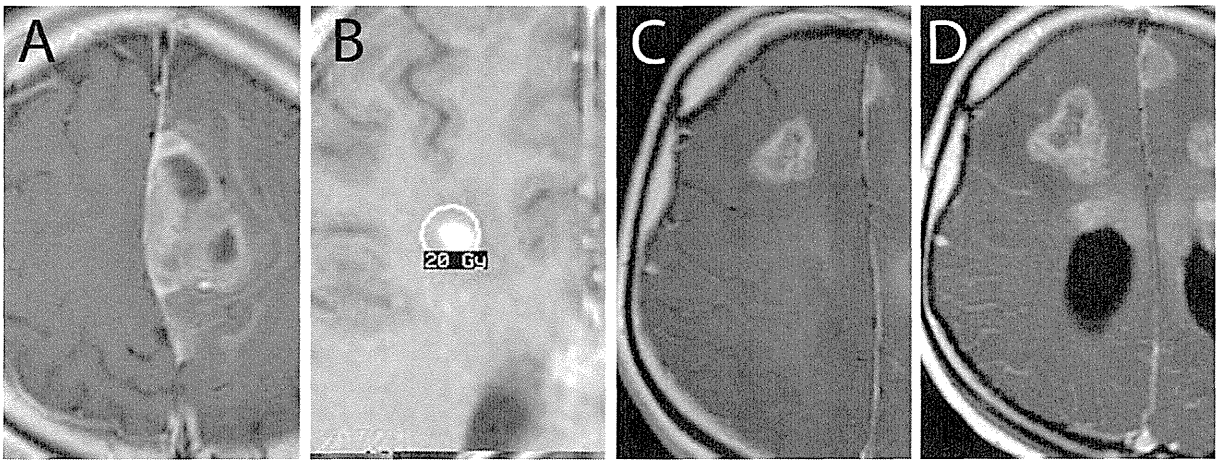

Figure 1. Case 7 in Table 1 is shown: (A) axial gadolinium-enhanced T1-weighted magnetic resonance imaging (MRI) at presentation; (B) dose planning of stereotactic radiosurgery for recurrence; (C, D) MRI taken at 1 (C) and 3 months (D) after stereotactic radiosurgery showing tumor progression.

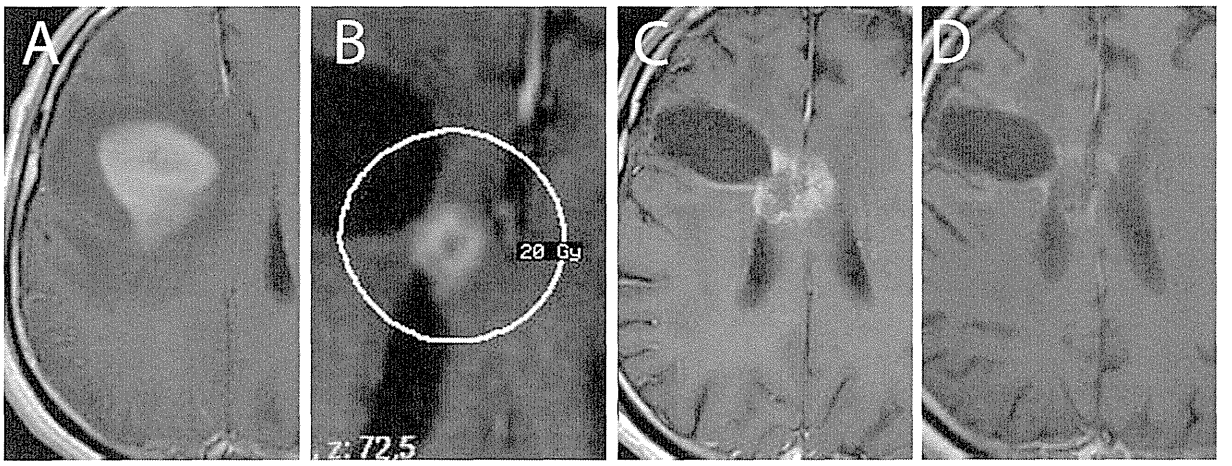

Figure 2. Case 1 in Table 2 is shown: (A) axial gadolinium-enhanced T1-weighted magnetic resonance imaging (MRI) at presentation; (B) dose planning of stereotactic radiosurgery for recurrence; (C) MRI taken at 1 month after stereotactic radiosurgery showing diffuse enhancement around treated lesion; (D) MRI taken at 25 months after stereotactic radiosurgery showing no recurrence.

which temozolomide at a dose of 200 mg/m^2 using the 5 of 28-day regimen was initiated. After the third cycle of temozolomide, eruption and thrombocytopenia were observed, so chemotherapy was switched to nimustine hydrochloride (100 mg/dose), which was administered intravenously once a month thereafter. Although complete remission was maintained until 17 months after the onset, a recurrent lesion 10 mm in diameter was observed near the resection cavity in the right frontal lobe. Extended field SRS was applied to this lesion. The clinical target volume was set as the gadolinium-enhanced lesion plus a 1-cm–wide margin, and 20 Gy was prescribed at the margin of this wide target (Fig. 2B). One month after the SRS, diffuse enhancement around the irradiated area was observed (Fig. 2C). As radiation necrosis was suspected, oral prednisolone at a dose of 30 mg daily was initiated, and the area of enhancement ceased to expand thereafter. At 25-month follow-up after the SRS, the treated lesion had been locally controlled, and no new recurrence was noted (Fig. 2D).

A 27-year-old man (case 2 in Table 2) presented with right hemiparesis. MRI revealed a homogeneously enhanced mass in the right frontal lobe (Fig. 3A). Stereotactic biopsy was performed, and the diagnosis of glioblastoma was obtained. He received 60-Gy external beam radiotherapy followed by adjuvant temozolomide at a dose of 200 mg/m^2 using the 5 of 28-day regimen. Complete remission was achieved and maintained until 39 months after the onset, when a recurrent lesion (maximal diameter, 15 mm) was noted in the right frontal lobe